



HAL
open science

Surface Wave Tomography of the Alps Using Ambient-Noise and Earthquake Phase Velocity Measurements

Emanuel D. Kästle, A. El-Sharkawy, L. Boschi, T. Meier, C. Rosenberg, N. Bellahsen, L. Cristiano, C. Weidle

► **To cite this version:**

Emanuel D. Kästle, A. El-Sharkawy, L. Boschi, T. Meier, C. Rosenberg, et al.. Surface Wave Tomography of the Alps Using Ambient-Noise and Earthquake Phase Velocity Measurements. *Journal of Geophysical Research: Solid Earth*, 2018, 123, pp.1770-1792. 10.1002/2017JB014698 . insu-03595931

HAL Id: insu-03595931

<https://insu.hal.science/insu-03595931>

Submitted on 3 Mar 2022

HAL is a multi-disciplinary open access archive for the deposit and dissemination of scientific research documents, whether they are published or not. The documents may come from teaching and research institutions in France or abroad, or from public or private research centers.

L'archive ouverte pluridisciplinaire **HAL**, est destinée au dépôt et à la diffusion de documents scientifiques de niveau recherche, publiés ou non, émanant des établissements d'enseignement et de recherche français ou étrangers, des laboratoires publics ou privés.

Copyright

RESEARCH ARTICLE

10.1002/2017JB014698

Key Points:

- Different types of surface wave measurements are combined to create a 3-D shear velocity model of the Alpine lithosphere
- The presented surface wave method allows to resolve subduction slabs in the uppermost mantle
- The model shows evidence for slab detachments under the western and eastern Alps

Supporting Information:

- Supporting Information S1
- Data Set S1

Correspondence to:

E. D. Kästle,
emanuel.kaestle@upmc.fr

Citation:

Kästle, E. D., El-Sharkawy, A., Boschi, L., Meier, T., Rosenberg, C., Bellahsen, N., ... Weidle, C. (2018). Surface wave tomography of the Alps using ambient-noise and earthquake phase velocity measurements. *Journal of Geophysical Research: Solid Earth*, 123, 1770–1792. <https://doi.org/10.1002/2017JB014698>

Received 12 JUL 2017

Accepted 19 JAN 2018

Accepted article online 25 JAN 2018

Published online 28 FEB 2018

Surface Wave Tomography of the Alps Using Ambient-Noise and Earthquake Phase Velocity Measurements

Emanuel D. Kästle¹ , A. El-Sharkawy^{2,3}, L. Boschi¹ , T. Meier², C. Rosenberg¹, N. Bellahsen¹, L. Cristiano², and C. Weidle² 

¹Sorbonne Université, CNRS-INSU, Institut des Sciences de la Terre Paris, Paris, France, ²Institut für Geowissenschaften, Christian-Albrechts-Universität, Kiel, Germany, ³National Research Institute of Astronomy and Geophysics, Helwan, Cairo, Egypt

Abstract A large data set of surface wave phase velocity measurements is compiled to study the structures of the crust and upper mantle underneath the Alpine continental collision zone. Records from both ambient-noise and earthquake-based methods are combined to obtain a high-resolution 3-D model of seismic shear velocity. The applied techniques allow us to image the shallow crust and sedimentary basins with a lateral resolution of about 25 km. We find that complex lateral variations in Moho depth as mapped in our model are highly compatible with those obtained from receiver function studies; this agreement with entirely independent data is a strong indication of the reliability of our results, and we infer that our model has the potential to serve as reference crustal map of shear velocity in the Alpine region. Mantle structures show nearly vertical subducting lithospheric slabs of the European and Adriatic plates. Pronounced differences between the western, central, and eastern Alps provide indications of the respective geodynamic evolution: we propose that in the southwestern and northeastern Alps, the European slab has broken off. The complex anomaly pattern in the upper mantle may be explained by combination of remnant European slab and Adriatic subduction. Along-strike changes in the upper mantle structure are observed beneath the Apennines with an attached Adriatic slab in the northern Apennines and a slab window in the central Apennines. There is also evidence for subduction of Adriatic lithosphere to the east beneath the Pannonian Basin and the Dinarides down to a maximum depth of about 150 km.

1. Introduction

The evolution of the Alpine region is characterized by the creation, subduction, and collision of rather small and mobile microplates caught between the larger Eurasian and African plates that are slowly converging since about 85 Ma (Handy et al., 2010; Stampfli & Borel, 2002). This configuration results in a highly variable subduction and collision history compared, for example, to Pacific subduction zones and the Himalayan continental collision zone as evident already from the small dimensions and the strong curvature of the Alps (Figure 1).

Because of the absence of intermediate-depth seismicity in the Alps (International Seismological Centre, 2014), the slabs can only be resolved by seismic imaging. Resolving the highly variable crust and small slab segments in the mantle lithosphere represents, however, a challenge. Large-scale *P* wave travel time tomography shows convincing evidence for the presence of slabs beneath the Alps, in some parts down to the mantle transition zone (Giacomuzzi et al., 2011; Koulakov et al., 2009; Li et al., 2008; Piromallo & Morelli, 2003; Spakman & Wortel, 2004). The high-resolution model by Lippitsch et al. (2003) is obtained by local *P* wave travel time tomography with careful crustal corrections. It shows in the western-central Alps a Eurasian slab subducting steeply to the SE and a NE dipping Adriatic slab in the eastern Alps with a slab gap between these segments. Furthermore, there is evidence for horizontal slab tearing in the western Alps. The view that Adriatic and not Eurasian lithosphere is subducting in the eastern Alps has been opposed by Mitterbauer et al. (2011), on the grounds that high-resolution models do not include the forelands, and consequently, the continuation of the mantle lithosphere into the forelands has not been resolved unambiguously yet. Similarly, slab tearing (Lippitsch et al., 2003) in the western Alps has recently been questioned by Zhao et al. (2016).

The combination of *P* and *S* wave velocity models is needed to distinguish between compositional and temperature-related anomalies (Giacomuzzi et al., 2012; Goes et al., 2000). Intermediate-resolution, regional *S*

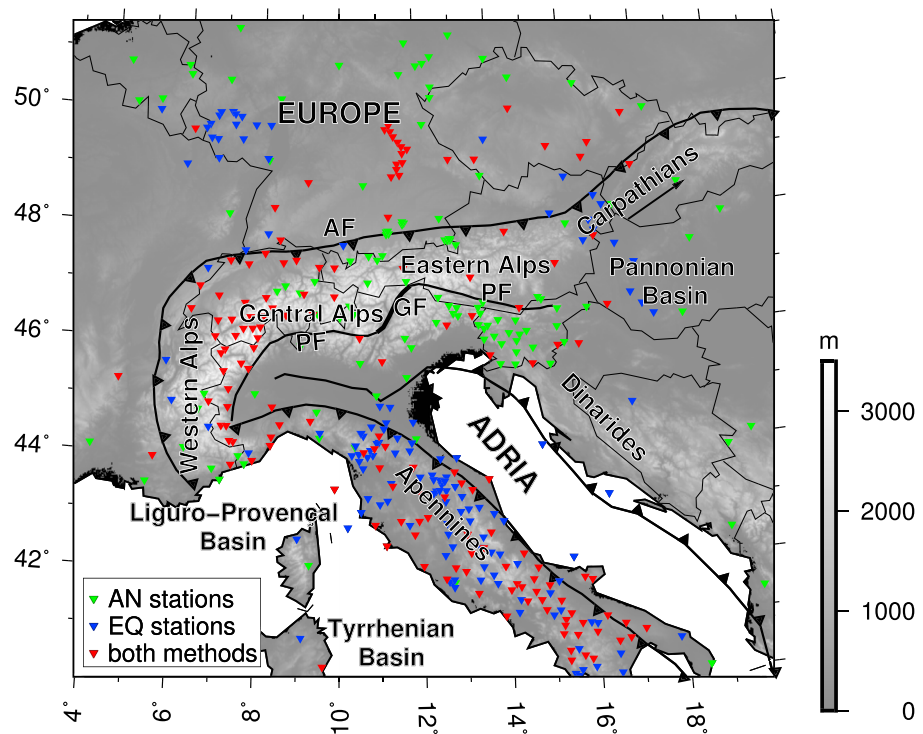


Figure 1. Map of the main tectonic units involved in the Alpine continental collision. Triangles show the locations of the stations and colors indicate in which data set they are used. AF = Alpine frontal thrust; PF = Periadriatic Fault; GF = Giudicarie Fault. Tectonic boundaries from Faccenna et al. (2014).

wave velocity models have been derived by inversions of surface wave dispersion (Meier et al., 2016), surface wave dispersion and *S* wave travel times (Auer et al., 2014), waveform inversions of regional seismic events (Zhu et al., 2012), or waveform inversions of regional and teleseismic events (Legendre et al., 2012). Because of the limited occurrence of local earthquakes in time and space in the Alpine region and the limited resolution of teleseismic body wave tomography in the lithosphere, in most of these studies surface wave data are inverted, alone or jointly with other data sets. The resulting models resolve the main properties of the upper mantle in the forelands beneath Adria, central Europe, the Pannonian Basin, and the Ligurian Sea, but the resolution in the Alpine region remains limited. *S* wave velocity models of higher resolution have been determined by inversion of surface wave phase velocities obtained from ambient-noise (AN) studies. For the Alpine region, isotropic (Verbeke et al., 2012) and anisotropic (Fry et al., 2010) phase velocity maps have been calculated. Molinari et al. (2015) present an isotropic 3-D crustal model for the Alps from AN.

Kästle et al. (2016) show, using existing data for the Alpine region, that surface wave analyses of earthquake (EQ) and AN records are compatible in the period range between about 10 s and 35 s. AN signals are mainly composed of short period surface waves, thus being most sensitive to shallow structures (crust). EQ-based surface wave measurements yield information at a broad range of periods up to more than 250 s, hence being essential to resolve the mantle lithosphere, the lithosphere-asthenosphere boundary (LAB), slab segments, and the asthenosphere.

The crust of the Alps has been widely studied by active seismic soundings along several transects (EGT: Pfiffner (1992); ECORS-CROP: Bois and Party (1990); Hirm et al. (1989); Hirm et al. (1987); Roure et al. (1996); NFP20: Pfiffner et al. (1997); TRANSALP: Bleibinhaus and Gebrande (2006); Castellarin et al. (2006); Lüschen et al. (2004); TRANSALP Working Group et al. (2002); Western Alps: Thouvenot et al. (2007); Eastern Alps: Oeberseder et al. (2011)), by passive local *P* wave tomography (Béthoux et al., 2007; Diehl et al., 2009) and receiver function studies (Lombardi et al., 2008; Kummerow et al., 2004; Zhao et al., 2015). These studies show that the crust thickens to more than 50 km on the Eurasian side of the Alpine suture, with a very sharp step of about 20 km across the suture in the western and central Alps. In the eastern Alps, the Moho transition from one plate to the other appears to be smoother and the plate boundaries are thus harder to identify (e.g., Spada et al., 2013). Diehl et al. (2009) resolve lateral and vertical *P* wave velocity gradients in the crust, and Spada et al. (2013)

study the Moho topography by combining passive and active methods. In the eastern Alps, the sparse station coverage, however, results in relatively poor resolution. A comparable *S* wave velocity model for the crust is not yet available. Receiver function and active seismic studies show that the deeper parts of the crust as well as the mantle lithosphere possess a complicated structure that is not clearly resolved yet (Lombardi et al., 2008; Oeberseder et al., 2011; Spada et al., 2013; Thouvenot et al., 2007).

Surface wave tomography, as conducted in this study, provides structural information complementary to local earthquake tomography and teleseismic body wave tomography. The application of local earthquake tomography is mainly restricted to the crust because most slabs in the Alps are seismically inactive (International Seismological Centre, 2014). The vertical resolution of the teleseismic body wave method is limited in the lithosphere and asthenosphere as a result of nearly vertical raypaths at these depths. Because of their high sensitivity to depth variations of velocities, surface waves are well suited to study properties of the crust, the Moho depth, the mantle lithosphere, the LAB, and the asthenosphere.

In this study, we combine shorter-period phase velocity dispersion measurements from AN cross-correlation functions with longer-period phase velocity dispersion data from EQ surface wave single- and two-station analysis. We next calculate 2-D maps of Love and Rayleigh phase velocity at different periods independently. Phase velocity maps provide the local phase velocity dispersion curve for each geographical grid node on the map. Each of these local dispersion curves is inverted individually for a 1-D shear velocity model using a fully nonlinear direct-search algorithm (Wathelet, 2008). Finally, the resulting 1-D shear velocity models are combined to construct a 3-D shear velocity model.

The AN and EQ observation methods are effective over overlapping, but different frequency bands (Kästle et al., 2016), so that our new, joint database includes an extremely broad band of surface wave frequencies; as different surface wave frequencies are sensitive to different depth ranges, this in turn helps to constrain structures over a greater range of depths. This approach has been applied in different parts of the Earth (e.g., Kohler et al., 2012; Shen et al., 2013; Ward et al., 2016; Yang, Li, et al., 2008; Yang, Ritzwoller, et al., 2008; Zhou et al., 2012), but ours is the first joint EQ-AN inversion for the Alpine structure. We accordingly consider this study to represent a significant progress with respect to earlier, similarly minded efforts (Fry et al., 2010; Molinari et al., 2015; Stehly et al., 2009; Verbeke et al., 2012).

2. Data Sets

2.1. Ambient-Noise Measurements

We compile a phase velocity dispersion data set for both Rayleigh and Love waves by cross correlation of AN records of station couples in central Europe. Our raw data cover the years 2007, 2008, 2012, and 2013 including a total of 313 stations. For each station couple, records are split into Z (vertical), R (radial), and T (transverse) components which are correlated separately to obtain the phase velocity dispersion for Rayleigh (from Z and R components) and Love waves (T components). The cross-correlation spectra are related to the phase velocity according to Aki (1957) and the method of extracting the phase velocity at the zero-crossings is based on Ekström et al. (2009). We use a modified scheme for which preprocessing, cross correlation, and phase velocity determination are explained in Kästle et al. (2016). The data set comprises 32,874 Rayleigh Z phase velocity curves, 25,001 for Rayleigh R and 27,090 for Love. It covers periods between 4 and 75 s; most measurements are obtained between 8 and 30 s (Figure 2).

We estimate the average error of our measurements by comparing station triplets, which are located on the same great-circle path (Figure 3). For each of these triplets, we use the phase velocity measurement from the most distant pair of stations and compare it to the average of the two shorter-path measurements, weighted according to station-station distance (Lin et al., 2008). The differences can be used as proxy for the random error in our phase velocity estimations. We show in Figure 3 that for most of our data, the difference between long- and short-path measurements is around 0.05 km/s. The deviations increase at longer and shorter periods. For distances between 150 and 1,200 km, a trend can be observed, which indicates that short interstation distances give more reliable phase velocity estimations at short periods and vice versa.

Based on the error estimates so described, we find the average standard deviation of our Rayleigh wave measurements to be about 0.06 km/s at 25 s, increasing to 0.08 km/s at very short (<8 s) and long periods (>50 s). In the case of Love waves the same trend is observed, but standard deviations have larger maxima (0.1 km/s) at both ends of the period spectrum. This kind of misfit estimation does not entirely account for potential

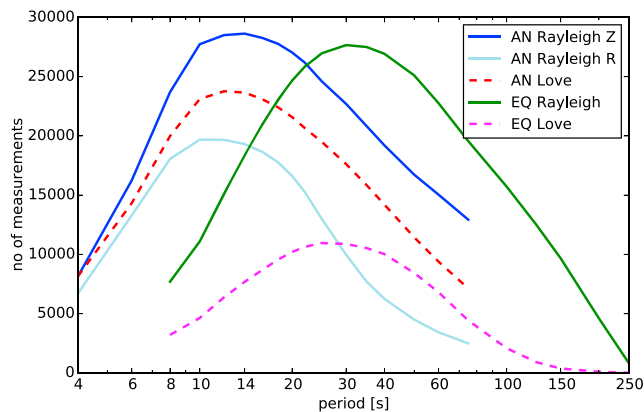


Figure 2. Number of measurements for the ambient-noise (AN) and the earthquake (EQ) two-station methods. Z and R refer to the component on which the phase velocity has been measured with the AN data.

errors due to nonuniformity of source distribution or media heterogeneity. A biased source distribution would affect both long- and short-path measurements, but the error would be reduced with increasing interstation distance.

2.2. Earthquake Two-Station Measurements

The “Two-Station Method” for measuring surface wave phase velocity is based on using earthquakes as signal sources (e.g., Kovach, 1978; Meier et al., 2004; Sato, 1955; Soomro et al., 2016); throughout this study, we accordingly refer to it as EQ-two-station method. An automated algorithm for interstation phase velocity measurements (Soomro et al., 2016) is applied to a large data set to obtain the fundamental-mode Rayleigh and Love phase velocities. We utilize a database consisting of more than 3,000 seismic regional and teleseismic events in the time period 1990–2015. The data are recorded by 387 broadband seismic stations distributed within and around the greater Alpine region (Figure 1) and are provided by the European Integrated Data Archive (WebDc/EIDA) and IRIS. For each station pair, approximately located on the same great-circle path or within 7° of

off-path propagation, the recorded waveforms are cross correlated and the dispersion curves of fundamental modes are calculated from the phase of the cross-correlation functions weighted in the time-frequency plane (Meier et al., 2004). The cross-correlation function is filtered with a set of frequency-dependent Gaussian band-pass filters and windowed in the time domain to minimize the effects from other signals. The automated selection of acceptable phase velocity measurements for each event is performed in the frequency domain based on a number of fine-tuned quality criteria including the difference to a 3-D path-specific reference model, smoothness, and the length of the selected dispersion curves (Soomro et al., 2016). To suppress the errors caused by the influence of lateral heterogeneity and off-path propagation, rejection of the perturbed interstation phase velocity measurements and averaging of many single-event measurements from both propagation directions are applied. Between 5 and 2,500 single-event dispersion measurements per interstation path are averaged, resulting in reliable broadband dispersion curves (and estimates of the associated uncertainty) representing the area of the Earth’s structure between the considered two stations with uncertainty estimates. In total, around 16,000 Rayleigh and 14,000 Love wave dispersion curves in the period

range (8–250 s) have been determined, with a standard deviation lower than 2% and standard errors lower than 0.6%.

A detailed comparison between phase velocity measurements obtained from the EQ-two-station and AN methods is given in Kästle et al. (2016). Dispersion measurements from both processing techniques are overall in very good agreement. At periods around about 30 s there is a slight discrepancy between AN and EQ measurements with the latter being a bit faster (0.05km/s). An analogous bias is also found and discussed by other authors (e.g., Yao et al., 2006). It may result from a stronger sensitivity of the earthquake data to scattering, especially from Moho topography, or from a lower resolution of the zero-crossing method when measuring phase velocities from AN at lower frequencies. Differences in structural sensitivities caused by different sensitivity kernels and the influence of higher modes could also explain this small discrepancy (Kästle et al., 2016; Yao et al., 2006).

2.3. Earthquake-Station Measurements

We add the global surface wave phase velocity data set of Ekström (2011) that includes first-order structures in central Europe between 22 and 250 s period and provides a good background model. These earthquake-station measurements have the least influence on the phase velocity maps because the travel time delays can be ascribed to velocity anomalies anywhere on the entire earthquake-station path. For the station-station measurement, the anomalies are concentrated on the shorter paths within

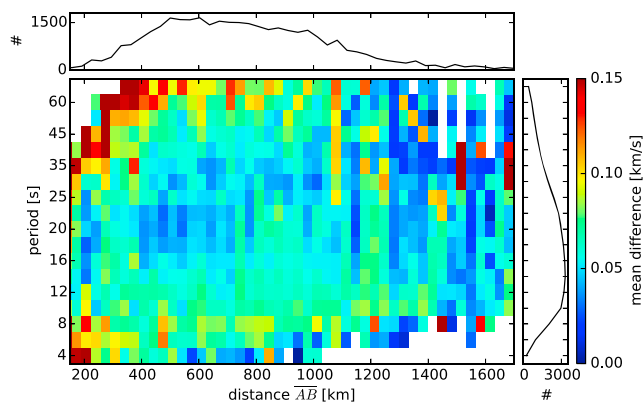


Figure 3. Estimation of measurement uncertainty of AN Rayleigh records by comparison of station triplets. We compare the phase velocity measurements between three stations (A, B, and C) along the same great-circle path. The difference in velocity between the outer stations (AB) and the path-weighted average phase velocity of the two shorter paths (AC and CB) is shown. We define that the great-circle deviation of the third station (C) must not be greater than 0.1°. This gives approximately 5,000 station triplets for the Rayleigh wave data set. The absolute differences between long- and short-path measurements are binned and averaged according to the period and distance of the long-path measurement. The curves at both sides of the plot give the number of measurements (#) used in this analysis.

the study region and have therefore a larger influence on each block of the inversion raster. Tests (not shown for brevity) indicate that the mapped phase velocity anomalies change significantly at the map borders by including the earthquake-station measurements but show only minor differences where the data coverage from the other methods is good (maximum 2% difference, in few parts of the model). By using this global data set, we aim to minimize the smearing effect at the model boundaries and in regions of sparse measurements.

3. Derivation of the Model

3.1. Phase Velocity Maps

We jointly invert dispersion measurements from the three mentioned data sets to derive phase velocity maps (e.g., Boschi & Dziewonski, 1999) at different periods. The AN dispersion curves are smoothed before inversion by fitting a fifth-order polynomial to the data. This is justified by the fact that jumps in the dispersion curves are unrealistic given the depth averaging properties of the surface wave dispersion. These jumps are caused by noise in the cross-correlation spectra and errors in the automated picking of the curves. The EQ two-station method provides smooth phase velocity curves by averaging over two-station measurements from several events (Soomro et al., 2016).

The study region is subdivided in a 0.1×0.1 (great circle) degree raster, which is the same for all periods and for both Love and Rayleigh waves. We use a ray-theoretical approach for the signal propagation between each station couple along a great-circle path. This approach does not take into account the finite-frequency effects and multipathing propagation of surface waves, thus leading to errors in the resulting phase velocity maps. However, we expect to be small, based, for example, on the results of Boschi (2006). For the EQ two-station measurements, path-averaged dispersion curves are obtained by averaging the smooth parts of a large number of single-event dispersion curves using sources on both sides of the station pair (Soomro et al., 2016). This maximizes the sensitivity along the interstation path and minimizes it closer to the source (de Vos et al., 2013). The high consistency between AN and EQ dispersion curves at long periods (Kästle et al., 2016) indicates that the structural sensitivities are similar and indeed the ray approach is an appropriate approximation. Nevertheless, at long periods, future studies may profit from taking finite frequency effects into account.

The inversion is based on an iterative, linear least squares algorithm (LSQR, Paige & Saunders, 1982). It is regularized according to the criteria of Boschi and Dziewonski (1999); we use only roughness damping and no norm damping. We increase the roughness damping with period to account for the structural averaging properties of long period waves, so that mapped structures should not be smaller than half a wavelength. Additionally, we tuned the damping parameters to show a maximum of consistency with known geological structures.

The Love and Rayleigh wave data sets compiled from the analysis of the three components (Z, R, and T) of the AN records are inverted jointly with the EQ measurements. Different weights are attributed to the data sets, so that the AN R component measurements are weighted lower than the Z component ones because of the difference in data quality. EQ two-station measurements are weighted higher, in order to balance between AN and EQ measurements. For Rayleigh waves, the relative weights are 0.8, 1.0, 1.5, and 5 for AN R component, AN Z component, EQ two-station, and EQ single-station measurements, respectively (Figure 4). More important for the influence on the phase velocity maps are, however, the number of data and the path coverage, so that the single-station measurements show the least influence on the mapped structures despite the larger weight. In case of Love waves, the weights are 1, 1, and 5 for AN, EQ two-station, and EQ single-station measurements, respectively (Figure 5). Changes in the presented weighing scheme only produce minor differences in the phase velocity maps.

For each phase velocity map we determine the misfit between our data and the model predictions and calculate the misfit standard deviation. We discard data with a misfit larger than 3 times the standard deviation as outliers, which is about 2% of the data, both for Love and Rayleigh waves. The inversion procedure is then repeated to obtain our final maps (Figures 4 and 5).

3.2. Resolution of Phase Velocity Maps

We perform checkerboard resolution tests for the Rayleigh phase velocity maps with block sizes of 2 and 0.5° (Figure 6). We add random Gaussian noise with a standard deviation of 0.1 km/s to the synthetic data. This value is taken as high-noise proxy (see section 2). Resulting from the very good raypath coverage, the blocks are reproduced accurately in the central regions of the model, showing the highest resolution

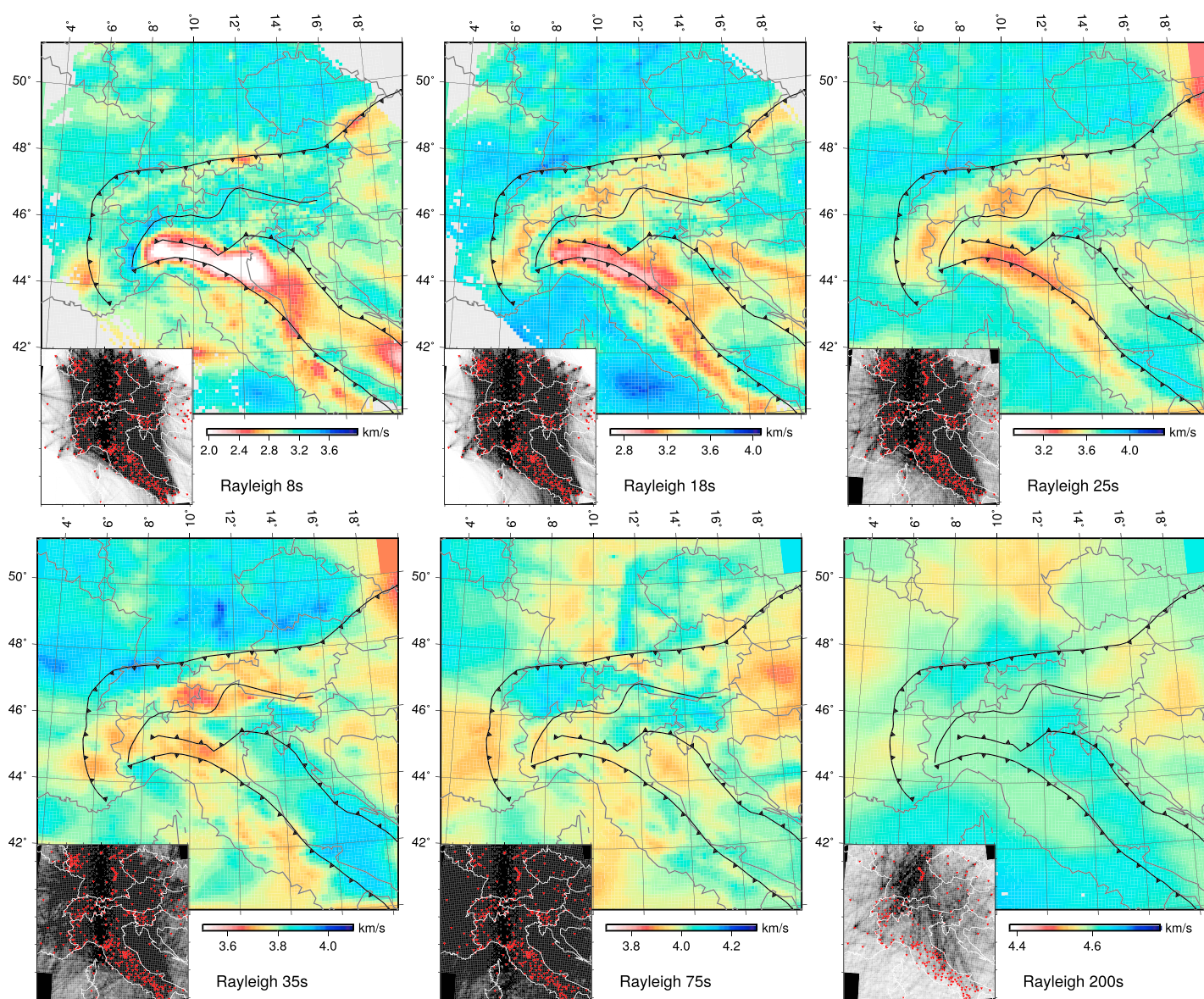


Figure 4. Rayleigh wave phase velocity maps at different periods. Blocks where less than three rays are passing are grayed out. The smaller map shows the path coverage for each block of the inversion raster.

in Switzerland and northwestern Italy. We are especially interested in the orogenic structures which are all in the high-resolution areas of our model apart from the southern Dinarides and beginning Carpathians (compare Figure 1). Some lateral smearing is expected in the southern Apennines and the eastern limits of the eastern Alps.

3.3. Depth Structure Inversion

From each cell of the phase velocity maps, we extract a dispersion curve for Rayleigh and Love waves, ranging from 4 to 250 s. We then use the neighborhood algorithm (Sambridge, 1999; Wathelet, 2008), a stochastic direct search, to find the best-fitting layered model for the P and S wave velocity (v_p and v_s). The model search is performed by randomly choosing 8,000 starting models from the solution space and calculating phase velocity dispersion curves for each of these models. For each model, a misfit estimate is calculated where we weight the Rayleigh wave misfit slightly higher than the Love wave misfit (1 versus 0.8). The reason for this is the larger amount of Rayleigh wave data and the lower measurement error (see section 2). The algorithm then continues to generate 200 new models in the parameter regions with the lowest misfit, which is repeated during 100 iterations giving a total of 28,000 models.

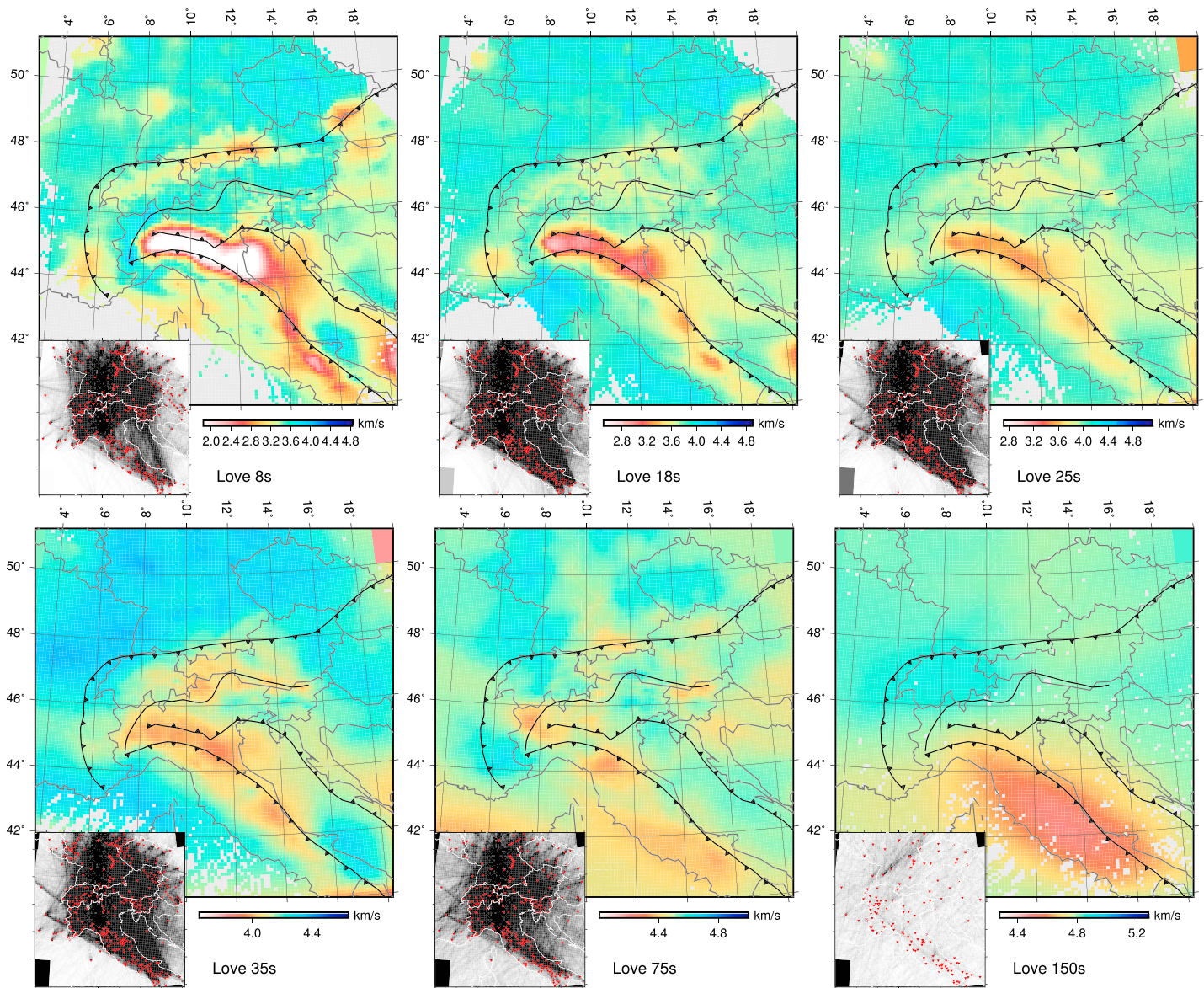


Figure 5. Love wave phase velocity maps at different periods. Blocks where less than three rays are passing are grayed out. The smaller map shows the path coverage for each block of the inversion raster.

The relative misfit of each modeled dispersion curve to the observed Rayleigh and Love wave velocity measurements is estimated according to equation (3.38) of Wathelet (2005):

$$\text{misfit} = \sqrt{\sum_{i=1}^{n_F} \frac{(x_{di} - x_{ci})^2}{x_{di}^2 n_F}}, \tag{1}$$

where n_F is the number of samples of the dispersion curve, x_{di} the data value of the i th sample, and x_{ci} the computed value. A misfit value of 0.03 therefore corresponds to 3% misfit between measured and modeled dispersion curves. The dispersion curves are sampled at an approximately logarithmic scale between 4 and 250 s, putting equal weights on short and long periods.

The model space is limited by giving a set of boundary conditions summarized in Table 1. We use a eight-layer model over a homogeneous half-space. The range of possible values for the upper three layers is chosen to represent approximately a sedimentary layer, upper, and lower crust. The three underlying mantle layers all have the same boundary values for v_p and v_s . The possible range of v_p/v_s is limited by the Poisson's ratios

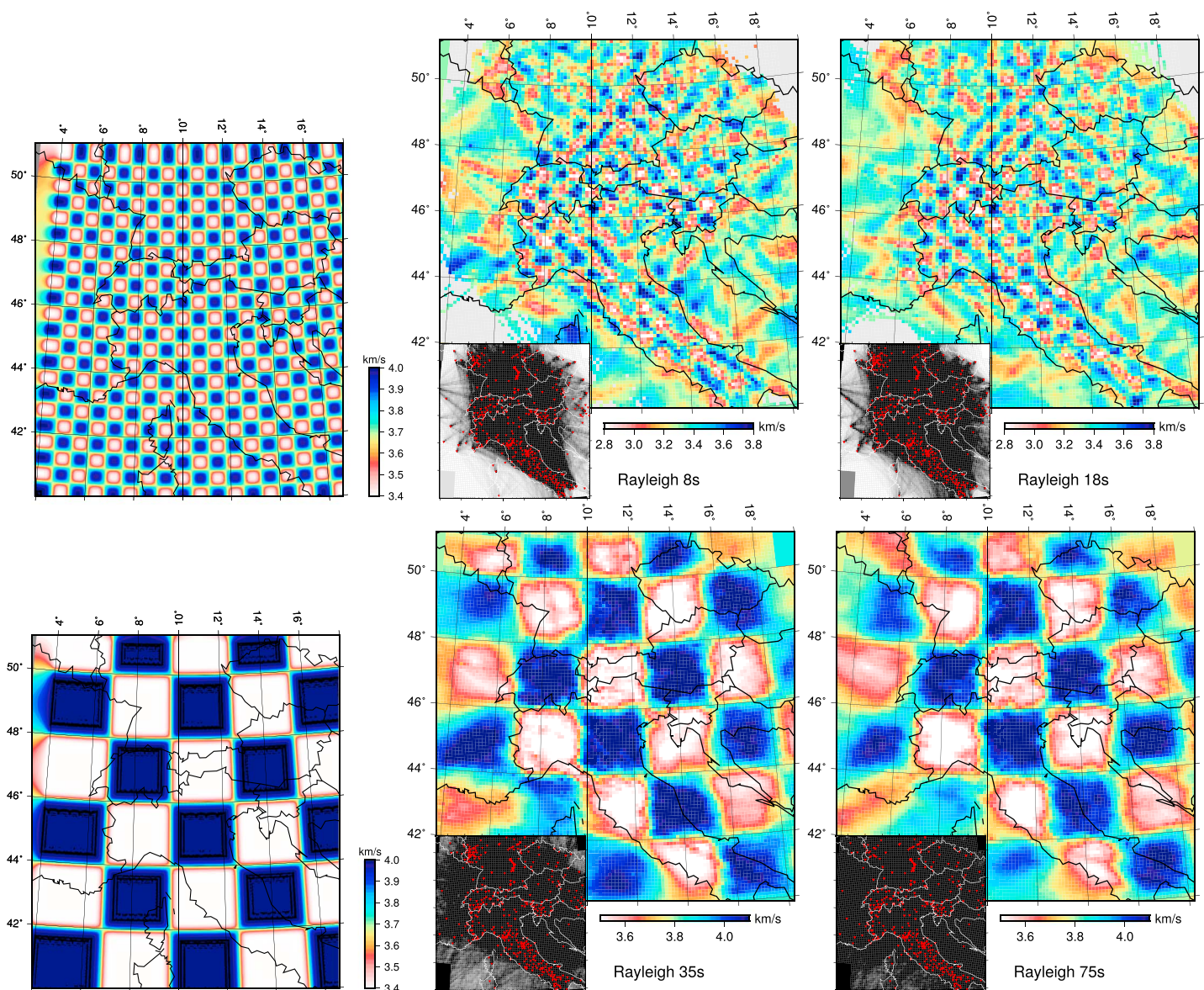


Figure 6. Checkerboard test for the Rayleigh phase velocity maps. The top panel shows an input model with 0.5° structure size. The recovered maps at 8 and 18 s are shown next to it, where noise with 0.1 km/s standard deviation has been added to the synthetic data. The smaller maps at the bottom of each figure show the path coverage for each block. The bottom panel shows the same for a 2° checkerboard model at 35 and 75 s.

that is allowed to vary between 0.2–0.5 in the crust and 0.2–0.4 in the mantle. The *P* velocity has no influence on the Love wave phase velocity and a minor influence on the Rayleigh wave phase velocity (Aki & Richards, 2002; Wathelet, 2005).

No density inversion is performed as its influence on the phase velocity dispersion is very low (Wathelet, 2005). No continuity between layers is required, so that both jumps to higher and lower velocities between layers are possible. The organization of the mantle layers follows loosely PREM, for example, by having a boundary around 220 km depth (Dziewonski & Anderson, 1981). The thickness of the crustal layer is determined by the model search. After the algorithm has obtained a first guess on the crustal thickness, the thicknesses of the mantle layers are fixed following two requirements: increasing layer thickness with depth and a boundary around 220 km depth (Table 1).

Within each of the seven top layers a linear velocity gradient is imposed, obtained by subdivision into five sublayers. In order to limit the number of free parameters and thus stabilizing the inversion, we only allow for positive velocity increments within the crustal layers. A negative velocity jump between layers is nevertheless

Table 1
Boundary Conditions Used in the Stochastic Model Search

Layer	Bottom depth (km)	v_p (km/s)	v_s (km/s)	Density (g/cm ³)	Velocity gradient
Sedimentary layer	0.1–12	1.6–6.8	0.8–3.0	2.400	Linear increase
Upper crust	5–50	5.0–7.2	2.8–4.3	2.750	Linear increase
Lower crust	10–95	6.0–7.2	3.5–4.2	2.900	Linear increase
Mantle layer 1	65–120	7.36–8.6	4.2–4.95	3.370	Linear
Mantle layer 2	130–170	7.36–8.6	4.2–4.95	3.375	Linear
Mantle layer 3	200–240	7.36–8.6	4.2–4.95	3.380	Linear
Mantle layer 4	270–310	7.5–9.6	4.4–5.2	3.481	Linear
Mantle layer 5	370–410	7.5–9.6	4.4–5.2	3.485	Uniform
Half-space		8.8–12.0	4.6–6.5	3.800	Uniform

Note. In the last mantle layer and the half-space, the velocities have no gradient within the layer.

possible. In the upper mantle layers, between the Moho discontinuity and 220 km depth, we allow also for linear decreasing velocities. This increases the complexity, but we are able to image the expected complex variations resulting from subducted lithosphere (Table 1).

The size of the sensitivity kernels of surface waves increases with period that influences the resolution of our model with respect to depth. By inverting Love and Rayleigh waves jointly, we improve the resolution as the two wave types have different sensitivity kernels.

In the following, we will only discuss v_s profiles because v_s is the best constrained parameter by Love and Rayleigh wave phase velocity dispersion (Wathelet, 2005). Our final model is obtained by calculating the average thickness and shear velocity for each layer of the 500 models with the lowest misfit. We therefore keep the sharp boundaries between layers, which is especially useful in order to interpret the Moho depth.

The *dinver* software package (Wathelet, 2008) that we employ does not allow for radially anisotropic layers in the solution model. This will introduce an error in the model, especially in the upper mantle where we expect pronounced radial anisotropy (Dziewonski & Anderson, 1981). The resulting isotropic 1-D model will therefore not exactly match Rayleigh and Love wave dispersion curves at the same time in the presence of radial anisotropy. We test for this effect by additionally performing separate model searches for Rayleigh and Love measurements. Rayleigh waves are mostly sensitive to v_{SV} and Love waves to v_{SH} (Muzyert & Snieder, 2000). By comparing the Voigt average (Babuska & Cara, 1991) of the resulting profiles to the joint-inversion results, we test whether our simplified approach introduces significant errors. We find that the imaged structures in the mantle only show minor differences, and we conclude that the errors from neglecting radial anisotropy are not influencing the presented interpretations of the slab geometries.

3.4. Depth Resolution Tests

We test the resolution capacities of the neighborhood search algorithm by creating synthetic dispersion curves for Love and Rayleigh waves from a simple model. In Figure 7 we show different models containing a sedimentary basin, a layered crust and underlying mantle, following PREM (Dziewonski & Anderson, 1981) apart from one smooth velocity anomaly. The anomaly has in all cases a peak of $\pm 4\%$ dv_s with respect to PREM. A random error with standard deviation of 0.1 km/s is added to the synthetic dispersion curves.

For each synthetic structural model in Figure 7, we calculate the Love and Rayleigh wave phase velocity and start a model search with the parameterization shown in Table 1. The range of tested models is shown as well as the final model, given by the layer average of the 500 lowest misfit models. The uncertainty of the Moho-depth estimation can be seen from the dashed lines in the profiles in Figure 7, which show the standard deviation range from the 500 best-fitting models. It becomes clear that the method is most sensitive to the shallow structure given that small deviations in the upper 10 km result in very high misfits. Thanks to the high sensitivity to and good resolution of short period waves, sedimentary basins and shallow crust are well constrained. Very complex crustal structures such as in Figure 7f cannot be uniquely resolved, which is caused by the decreasing resolution with depth and the nonuniqueness of the inverse problem.

The mean Moho depth shows an error of less than 2 km for the “simple” input models with strong contrast between crust and mantle velocities (Figures 7a and 7b). The tests show also that the resolution for a shallow

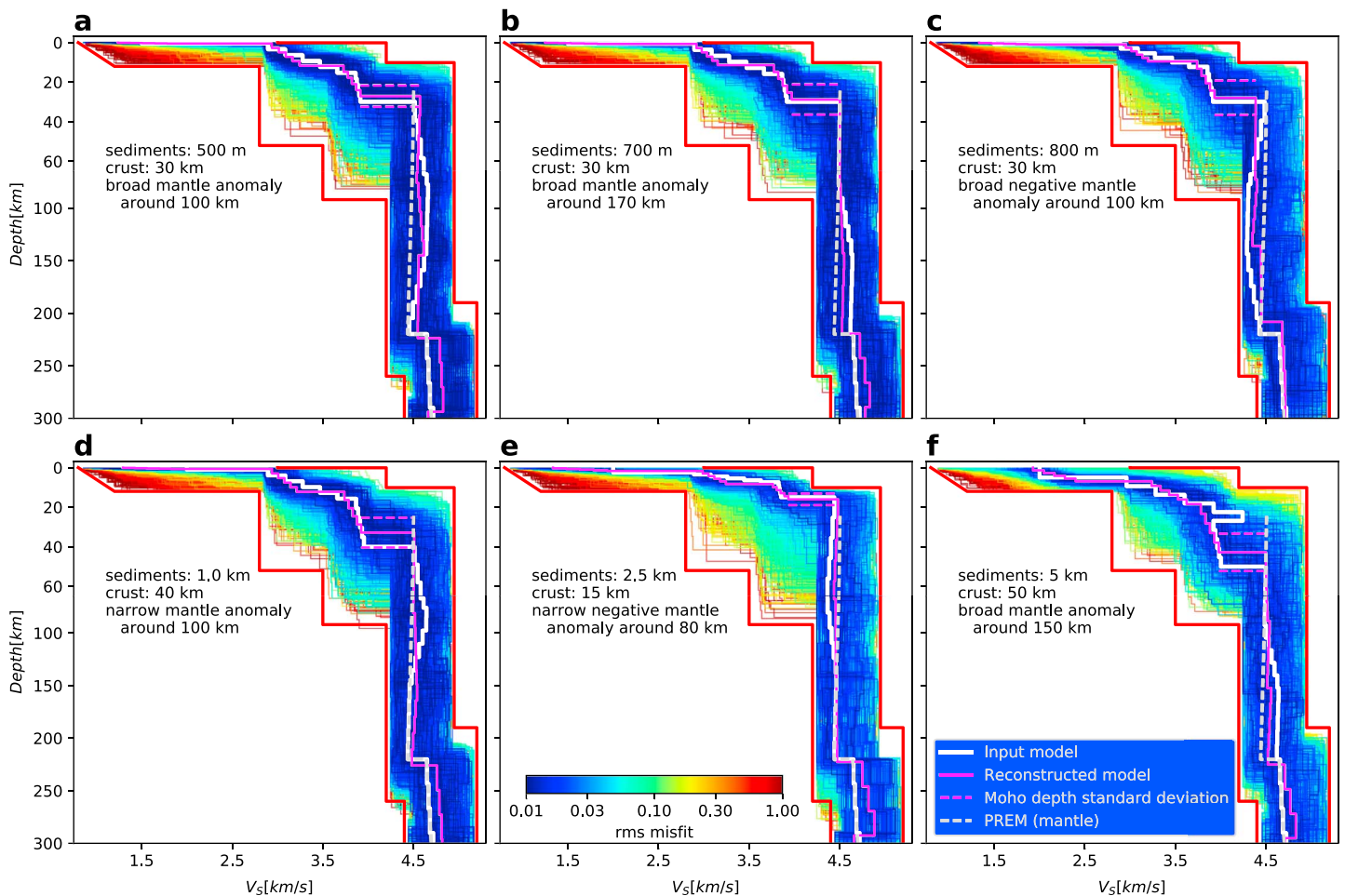


Figure 7. Tests showing the depth resolution of the applied method. Six different synthetic input models are compared to the recovered average of the 500 best-fitting models. The range of tested models is shown as color coded lines according to their misfit. Red boundaries give the limiting values for the model search from Table 1. Dashed pink lines show the uncertainty in the recovered Moho depth by giving the standard deviation.

Moho is much higher (Figure 7e). The depth uncertainty of the Moho is higher in the case of reduced velocities in the mantle, therefore reducing the crust-mantle contrast (compare Figures 7a and 7c). The Moho depth is not well resolvable in case of the high-velocity anomaly in the crust in Figure 7f.

Interestingly, the depth of the shallow sedimentary layers is well resolved, even though our surface wave observations do not include periods shorter than 4 s (which is relatively long with respect to typical sediment thicknesses). The depth error in most cases is less than 200 m but increases to 2 km for the 5 km basin. This suggests that a very thick sedimentary layer can result in a decreased resolution for deeper structure.

All mantle anomalies down to 220 km are recognized by the algorithm in their tendency (positive/negative velocity anomaly with respect to PREM). The peak amplitude is, however, always underestimated. Deeper (Figures 7b and 7f) and/or narrower (Figures 7d and 7e) anomalies are reconstructed with a larger error. The underestimation of the anomaly seems to cause some leakage into other depth ranges. This is, for example, visible in Figure 7b where the reconstructed velocities underneath the anomaly are too high. The shear velocity below 220 km tends furthermore to be overestimated in several of the presented models.

3.5. Model Misfit

We compare the dispersion curves from our measurements to the final models from the model search. The maps presented in Figure 8 give the relative misfit according to equation (1). Regions of higher misfit tend to correspond to thick sedimentary basins, for example, the Po Plain in northern Italy or the southeastern corner of Germany. This is presumably related to structural complexities (i.e., the basins and the associated sharp discontinuities) not being perfectly reproduced by our necessarily simplified model and also the higher standard

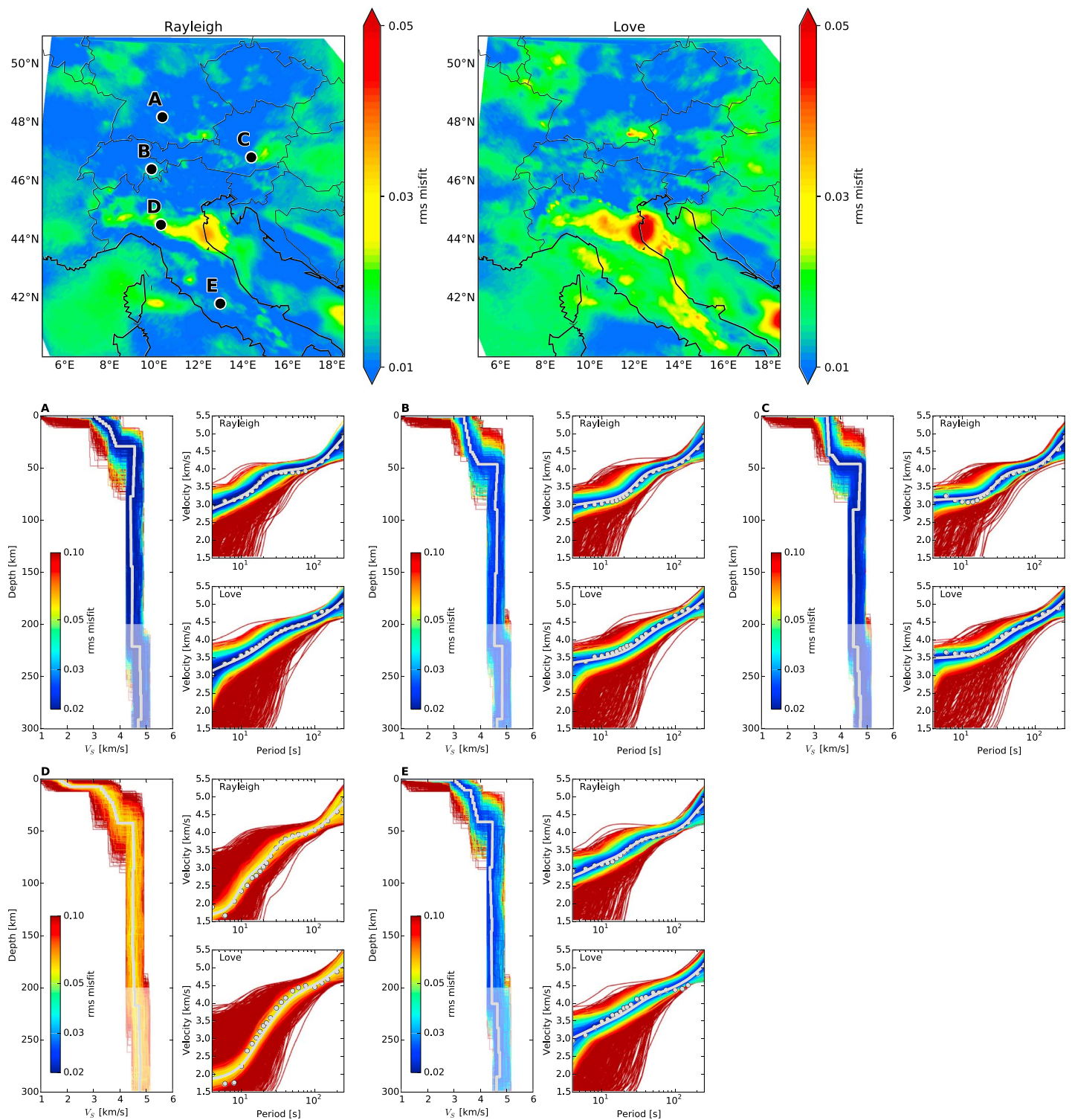


Figure 8. Maps show the relative misfit between the measured and modeled phase velocity curves, averaged over all periods. The labeled points in the map correspond to individual phase velocity curves shown below. Each panel shows the shear velocity models resulting from the model search and their corresponding misfit. The preferred model (gray) is the average of the 500 models with the lowest misfit. The corresponding dispersion curves for Love and Rayleigh waves are shown next to it. Gray dots show the data as extracted from the phase velocity maps.

deviation of the measurements at very high frequency (more sensitive to the sediment depth range). High standard deviations associated with potentially erroneous measurements can be seen in the high-frequency data in Figure 8 at location *D* (compare also section 2). We also observe a slight discrepancy between Love and Rayleigh wave phase velocities: in most cases, observed Rayleigh wave phase velocity is slightly slower than that computed from our model, while the opposite is true for Love waves (Figure 8). This could be an effect of radial anisotropy.

4. Shear Velocity Structure of the Alps

4.1. Crustal Structure

The individual solutions for all points of the raster give a 3-D structural model of the crust and mantle underlying the Alpine orogenic system. No smoothing is applied to the images so that each pixel in Figure 9 relates to one independent 1-D profile. Each of these profiles represents an average of the 500 best models that result from the model search (see section *Depth structure inversion*).

In Figure 9 we present the crustal structure from our model at different depth levels and in a set of cross sections. The shear velocity maps show the orogenic roots of the Alps, Apennines, and Dinarides with reduced velocity in the crust (20 km map, Figure 9) and elevated crustal thickness (45 km map, Figure 9). Also, the sedimentary basins can be identified in southern Germany and in the Italian Po Plain. The northern Alpine Molasse basin follows almost continuously the Alpine front from the Mediterranean to the Carpathians (compare also maps in Figures 4 and 5). From our model, its average depth is of 1 km in Switzerland and southern Germany and increases to 5 km in the southeastern corner of Germany. Previously reported results give a higher thickness in the Swiss Molasses Basin (3.5 km) but agree well with the sedimentary thickness in southeastern Germany (4.5 km) (Bigi et al., 1990). The cross sections show the wedge-like shape of the Po sedimentary basin in Italy with increasing thickness toward the south-east. The average thickness of the slow structure in our model is approximately 5 km and increases to 11 km toward the south and east. Increasing sedimentary thickness toward the south and maximum thicknesses of 3.5–9 km is also shown in the geologic map by Bigi et al. (1990).

The crustal sections presented in Figure 9 include the Moho-depth estimates of Spada et al. (2013), derived from receiver functions and controlled-source studies (CSS). The Moho depth in our model is defined by the inversion parameterization as the 4.2 km/s velocity limit (Table 1) and corresponds thus to the Moho in PREM (Dziewonski & Anderson, 1981). A good match, showing discrepancies of less than 5 km, is observed for the Moho depth of the European plate. In the model of Spada et al. (2013) the Adriatic Moho depth decreases to 10 km above the Ivrea body, an anomaly that is due to the presence of mantle material in the shallow crust (e.g., Schmid & Kissling, 2000) (profiles A–C between 250 and 400 km in Figure 9). The Ivrea body is represented in our model by anomalously high velocities between 0 and 25 km depth in profiles A–C. The mapped velocity anomaly is likely to be reduced in amplitude compared to the actual anomaly: according to the tests in Figure 7f, the applied inversion underestimates the strength of a fast and shallow crustal anomaly. Our models suggest that the Ivrea body is a rather continuous structure that follows the Periadriatic Fault from the junction with the Apenninic front in the south to 46°N. Its imaged size is therefore consistent with that inferred from previous studies of Schmid and Kissling (2000) or Diehl et al. (2009). The northernmost part of this fast anomaly is also spatially related to the Ticino gravity anomaly described by Kissling (1984).

The greatest crustal thickness is observed in profile A at the edge of the downgoing European plate. In combination with the fast Ivrea body signature on top of it, this could indicate underthrusting below the collisional wedge down to 60 km. This conclusion corroborates previous results based on receiver functions from a dense station profile (Zhao et al., 2015), showing that parts of the European crust may reach 80 km depth, overlain by the Ivrea body (Figure 10). Alternatively, the inferred Moho depth of 60 km in our model may be an expression of onsetting eclogitization of the root of the collisional wedge which would increase seismic velocities and is expected to occur at a depth of 55–60 km in the central Alps according to Bousquet et al. (1997). The Moho-depth estimation in our model may furthermore be influenced by the complex crustal structure for which the synthetic tests suggest an underestimation of the crustal thickness (Figure 7f). The crust may therefore extend even below 60 km in the Western Alpine collision zone.

The differences in Moho depth between our model and the one of Zhao et al. (2015) are of approximately 2 km for the European and 5 km for the Adriatic plate (Figure 10). We initially did not expect our surface wave model to reproduce weak velocity jumps within the crust, as the surface wave data are much better

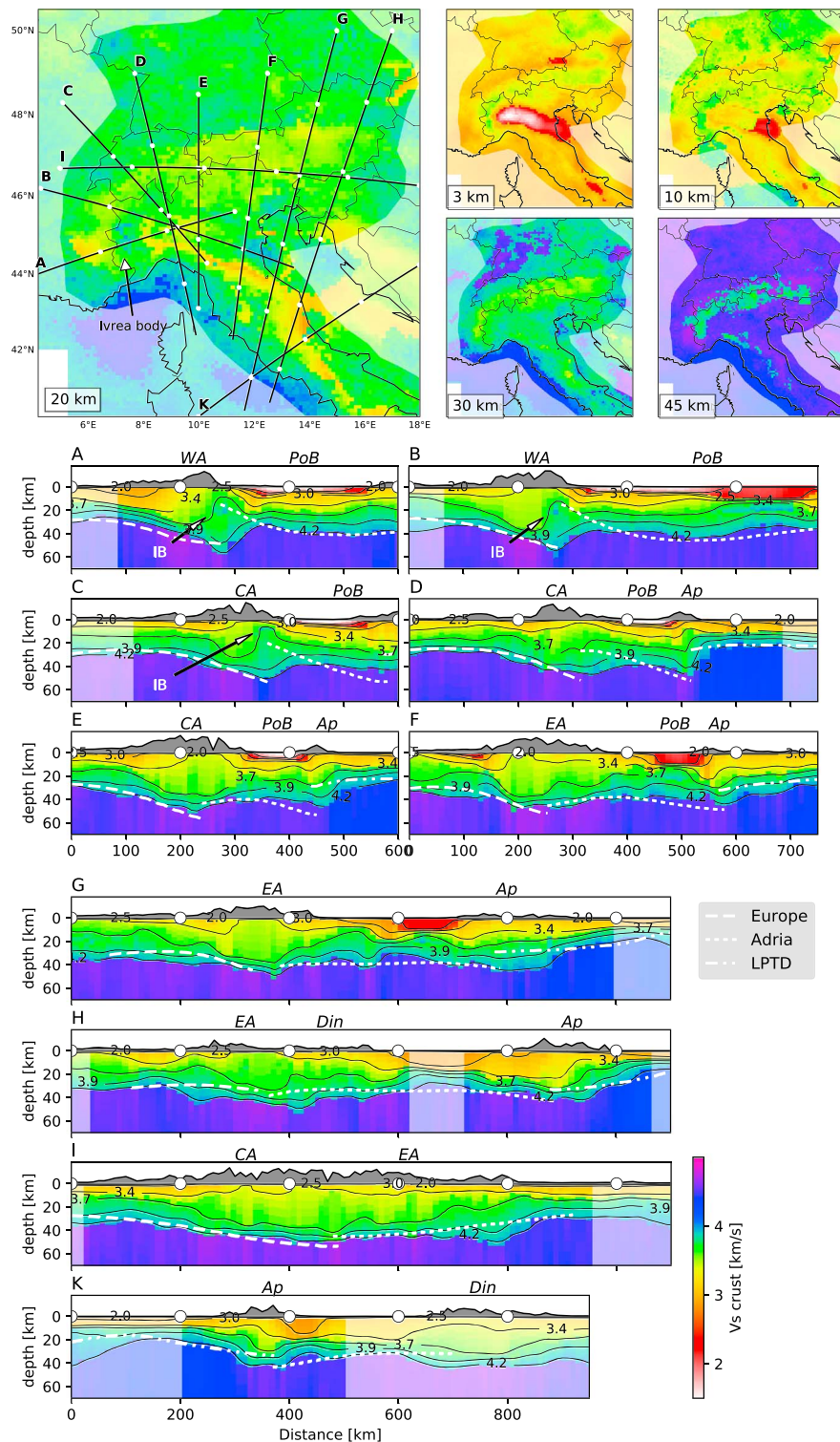


Figure 9. Crustal structure in map view and along 10 different cross sections. Each column in the cross sections represents the average of the 500 lowest misfit models from the model search. For an explanation of the dashed limits in the maps refer to Figure 1. Moho boundary lines in the cross sections for European and Adriatic plate and the Liguro-Provençal-Tyrrhenian Domain (LPTD) are taken from the receiver function and CSS study of Spada et al. (2013). IB marks the position of the Ivrea body. Regions of lower resolution are shown with reduced color intensities, according to the resolution tests in Figure 6. The abbreviations on top of each section refer to the topography: Ap = Apennines; CA = Central Alps; Din = Dinarides; EA = Eastern Alps; PoB = Po Molasse Basin; WA = Western Alps. The depth scale in the cross sections is exaggerated by a factor of 2.

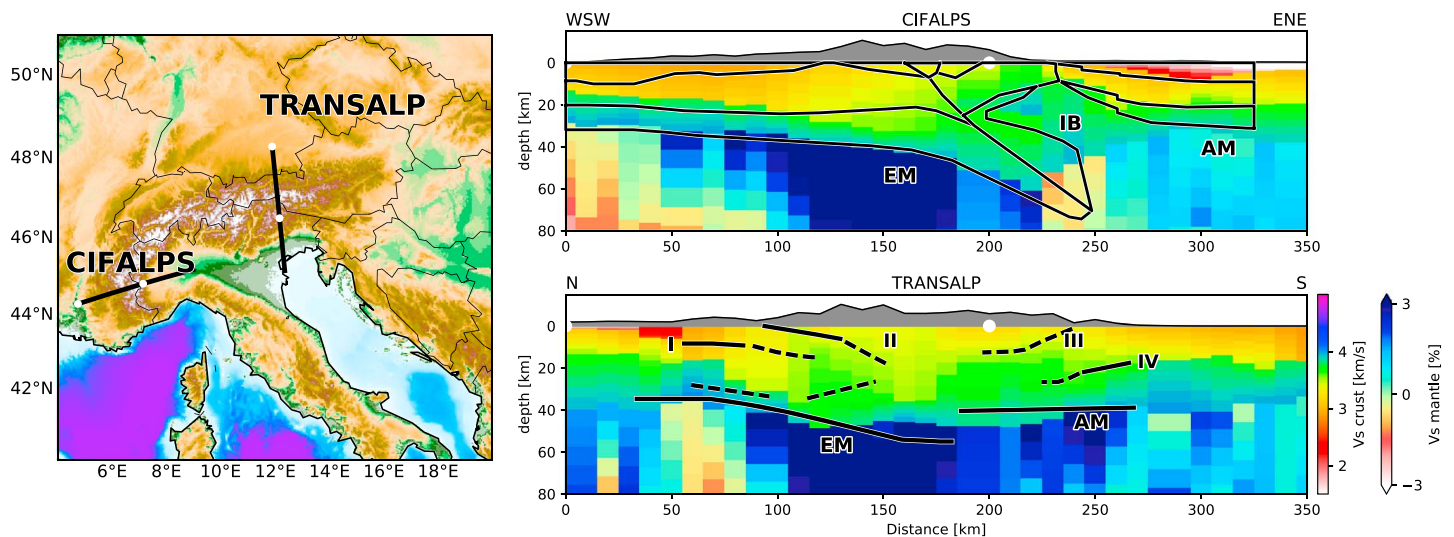


Figure 10. Comparison between the interpreted structures in the CIFALPS cross section from Zhao et al. (2015) and the TRANSALP cross section from Kummerow et al. (2004) (black lines) to our surface wave model. Mantle anomalies are shown as Voigt-averaged (Babuska & Cara, 1991) PREM deviations (Dziewonski & Anderson, 1981). The study of Zhao et al. (2015) is based on receiver functions; Kummerow et al. (2004) combine receiver function and reflection-seismic experiments. EM = European Moho; AM = Adriatic Moho; IB = Ivrea Body; I = Base of Mesozoic sediments; II = Sub-Tauern ramp; III = Sub-Dolomites ramp; IV = Adriatic intercrustal interface.

suit to constrain the average v_s structure than specific boundaries. However, our estimates of the depth of the sedimentary layer and of the upper crust agree well with receiver function results along the CIFALPS profile (Figure 10). The comparison between the receiver function and active-source study of Kummerow et al. (2004) and our model is also shown in Figure 10: the inferred intercrustal boundaries are only approximately reproduced by our model, but the Moho depth is in good agreement, with a maximum error of 8 km in the suggested area of the plate interface.

The Moho-depth map in Figure 11 shows a shallow Moho, especially in the Liguro-Provençal and Tyrrhenian basins, in agreement with the young age of oceanic crust there (e.g., Gueguen et al., 1997). Moho depths of 28 km along the Rhine-graben at 8°E, north of the Alps, are comparable to the results of previous studies and can be related to crustal thinning (e.g., Ziegler et al., 2004). The areas of greatest Moho thickness are related to the plate boundaries between Adria and Europe. The inferred present-day plate boundary in the Alps is thus closely confined to a zone striking immediately west and north of the Periadriatic Fault, in the western and central Alps, respectively. In the western Alps, the European Moho depth increases more gradually than the Adriatic one, indicating subduction of the European plate. In the central and eastern Alps the Moho topography of the Adria-Europe boundary is more symmetrically distributed.

4.2. Mantle Structure

We show in Figure 12 the shear velocity structure down to 200 km depth. We smooth the mantle structure both vertically and horizontally in order to make the structures easier to interpret which would otherwise show velocity fluctuations that are below our resolution limit (Figure 7). Stronger smoothing is applied to deeper structures in order to account for the fact that the depth sensitivity of surface waves is controlled by period (i.e., its wavelength). This is done by applying a different Gaussian 3-D filter at each depth level. The Gaussian filter width is approximated by 1/5 of the wavelength of a reference Rayleigh wave. The reference Rayleigh wave is the one that has its sensitivity maximum at this depth. An unfiltered version of the cross sections in Figure 12 is shown in the supporting information S1.

A clear distinction between regions of significantly higher shear velocity and regions of reduced velocities, most importantly the Liguro-Provençal, the Tyrrhenian and the Pannonian basins, and large parts of Germany, becomes evident in our maps of the mantle. At depths shallower than 100 km, the moderate fast anomalies are mainly due to cold continental lithosphere, while the strongest anomalies tend to follow the tectonic boundaries and are therefore interpreted as subducted lithosphere under the orogens that in most places continues into deeper parts of the mantle.

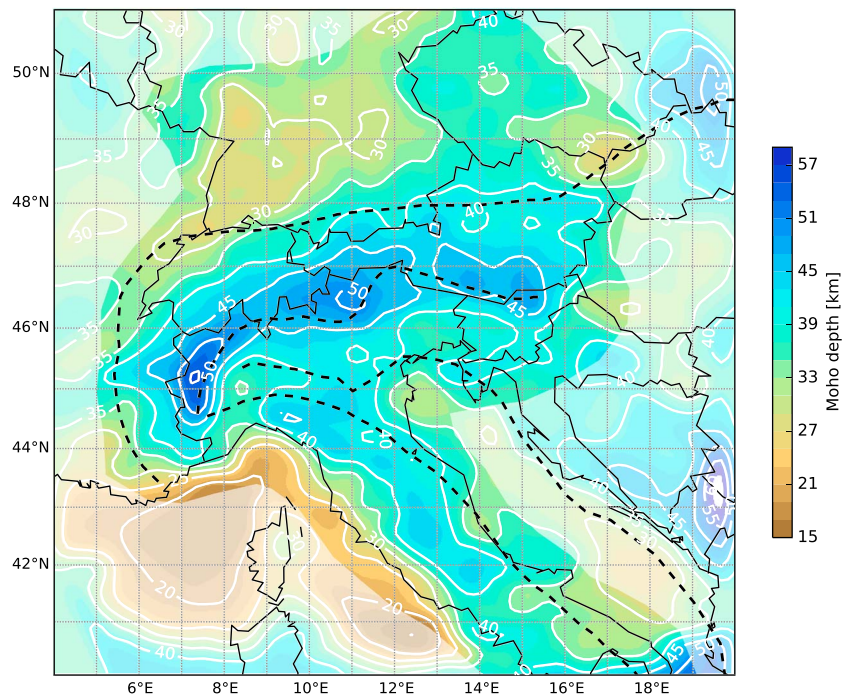


Figure 11. Moho depth map. The Moho depth is defined as average crustal thickness of the 500 best-fitting models (compare section 3.3). Regions of lower resolution are shown with reduced color intensities, according to the resolution tests in Figure 6. The dashed lines show the main tectonic boundaries (compare Figure 1).

Slow mantle velocities under the western Mediterranean can be explained by rollback subduction of the Ligurian oceanic plate below Eurasia that led to significant extension in the Liguro-Provençal and the Tyrrhenian basins (e.g., Gueguen et al., 1997). In the Pannonian Basin, an upwelling of the asthenosphere can explain the reduced velocities (e.g., Kovács et al., 2012). Lower velocities in the shallow mantle underneath Germany are also found by earlier studies (e.g., Koulakov et al., 2009) and are explained in terms of a shallower-than-average LAB and reduced velocities in the lithosphere (Geissler et al., 2010; Meier et al., 2016; Seiberlich et al., 2013).

Western Alps. A pronounced fast mantle anomaly is visible in cross-sections A and B of Figure 12 underneath the European plate, between the Moho and 80–100 km depth. A secondary moderate fast mantle structure at depth greater than 100 km extends along the same profiles in the distance range 300–600 km. The two anomalies are separated by a narrow low-velocity structure, especially visible in profile B, which follows approximately the Periadriatic Fault (Figure 12, compare also 100 km depth map).

The maps of Figure 12 show that in the shallow mantle (between 50 and 100 km), the Alpine high-velocity anomaly is laterally very continuous along the entire Alpine arc. At 100 km and deeper, however, the western Alpine anomaly is separated from the central Alpine one at about 46°N. The v_s anomaly is also not as pronounced and narrower compared to the central Alps.

We interpret the fast structure underneath the western Alps as European slab. The deeper mantle structure under the Po Basin in profiles A and B in Figure 12 is likely to be either a broken-off part of this European slab or the Adriatic slab or a mixture of both. Zhao et al. (2016) propose that a complex interaction between the eastward subducting European and the northward subducting Adriatic slabs results in the thick mantle anomaly under the junction between the western Alps and the Apennines. The location of the anomaly under the northern Apennines and the continuity with the rest of the Apenninic anomaly suggests that it is part of the Adriatic slab.

Central Alps. The cross-sections C–F in Figure 12 show a 100–150 km thick vertical high-velocity anomaly which we attribute to the European lithospheric plate because it is in continuity with the European Moho. Its northern and southern limit seems to correspond to the Alpine Front and the Periadriatic Fault, respectively. It is distinct from the western Alpine anomaly, which shows no pronounced vertical continuation below 100 km.

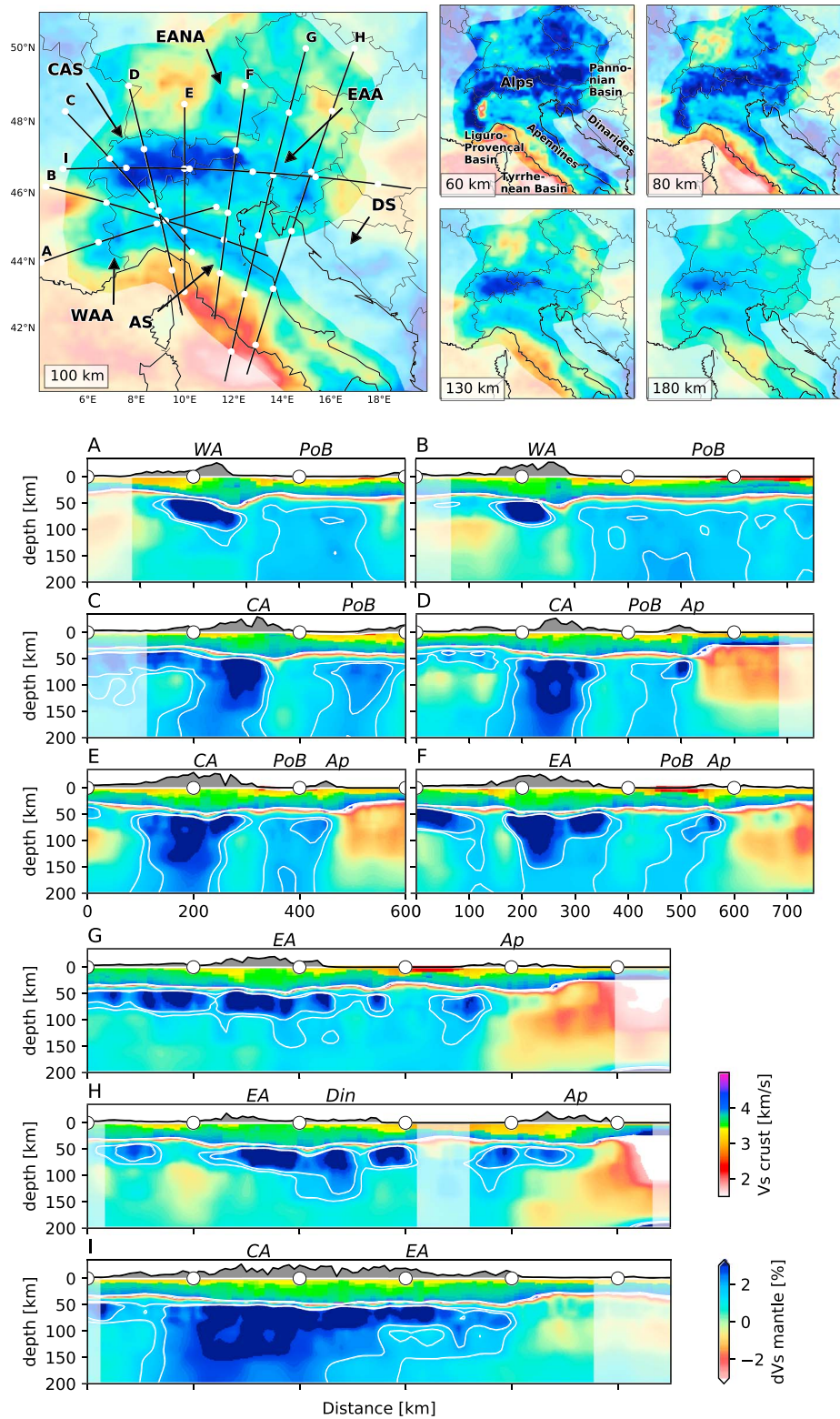


Figure 12. Shear velocity structure in map view and along 10 different cross sections as deviations from PREM (Dziewonski & Anderson, 1981). Regions of lower resolution are shown with reduced color intensities, according to the resolution tests in Figure 6. The +1.5% and +2.0% contour lines are shown to emphasize the slab anomalies. WAA = western Alpine anomaly; CAS = central Alpine slab; EANA = eastern Alpine northern anomaly; EAA = eastern Alpine anomaly; AS = Apenninic slab; DS = Dinaric slab. The abbreviations on top of each section refer to the topography: WA = western Alps; CA = central Alps; EA = eastern Alps; Ap = Apennines; Din = Dinarides; PoB = Po Molasse Basin.

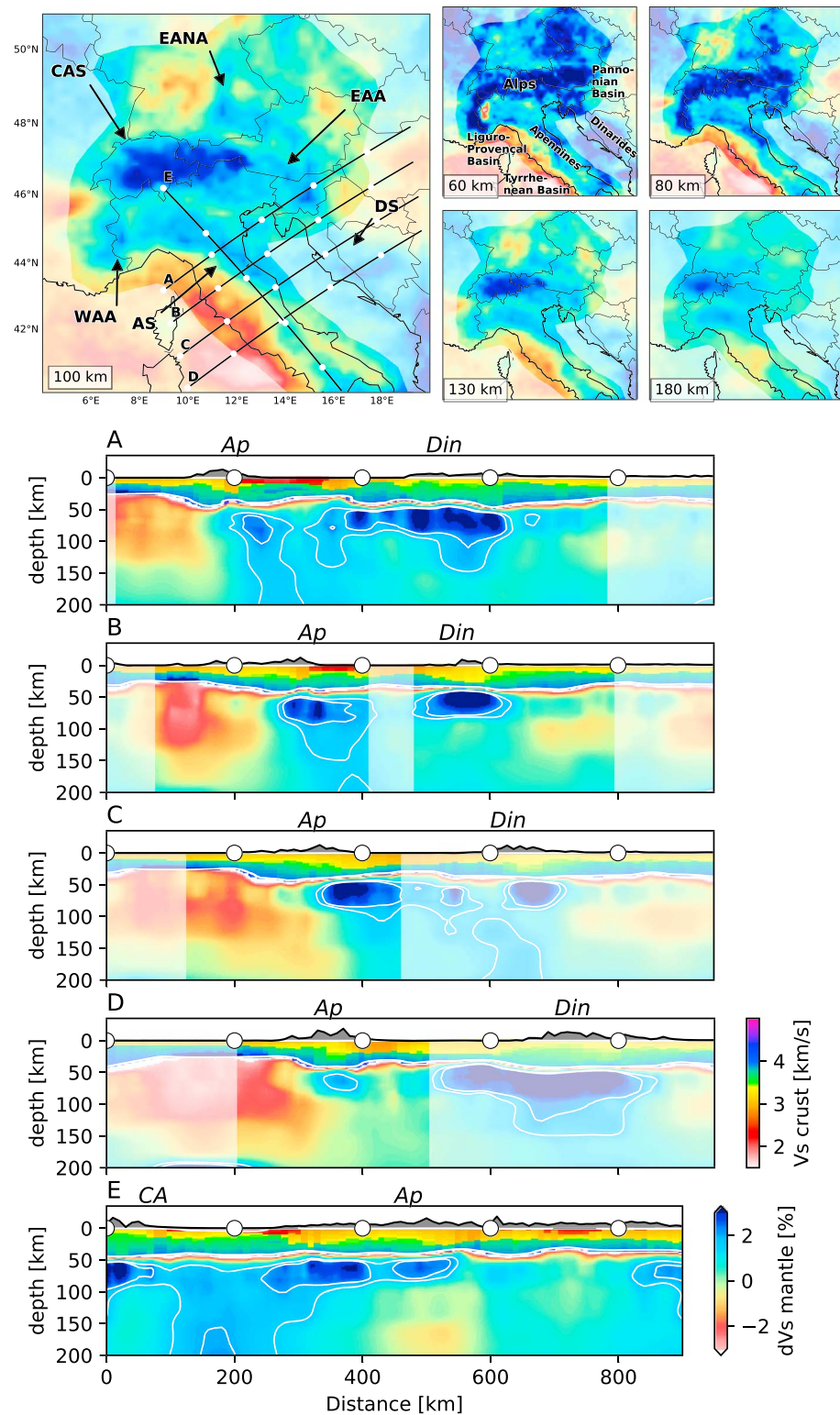


Figure 13. Shear velocity structure in map view and along five different cross sections through the Apennines and Dinarides as deviations from PREM (Dziewonski & Anderson, 1981). Regions of lower resolution are shown with reduced color intensities, according to the resolution tests in Figure 6. The +1.5% and +2.0% contour lines are shown to emphasize the slab anomalies. WAA = western Alpine anomaly; CAS = central Alpine slab; EANA = eastern Alpine northern anomaly; EAA = eastern Alpine anomaly; AS = Apenninic slab; DS = Dinaric slab. The abbreviations on top of each section refer to the topography: WA = western Alps; CA = central Alps; EA = eastern Alps; Ap = Apennines; Din = Dinarides; PoB = Po Molasse Basin.

At depth below 150 km, the central Alpine anomaly seems to be slightly northward dipping in profiles C and D (Figure 12). This could be a sign of an overturned slab. Also, in the Rayleigh wave phase velocity map the fast anomaly in the central Alps shifts gradually to the north with increasing period (Figure 5). This may, however, be caused by insufficient lateral resolution of our maps at very long periods, that is, large depths.

The thick high-velocity slab under the central Alps extends laterally, along the strike of the orogen, to about 12.5°E. At this point, the Periadriatic Fault is sinistrally offset along the Giudicarie Fault (see also Figure 1) and continues with reduced thickness and depth extent to almost 13°E. This can also be observed from the orogen-parallel cross-section I in Figure 12 at approximately 500 km distance along the profile.

Eastern Alps. The imaged fast anomalies in the eastern Alps are limited by the Pannonian Basin toward the east. They do not follow a pattern that is as clearly interpretable as in the western and central Alps, and the observed anomaly amplitudes are lower than in the central Alps. The main fast anomalies are located just north of the Periadriatic Fault and connect at 15°E to the Dinaric fast anomaly. A second fast anomaly, also subparallel to the Periadriatic Fault, is visible approximately 1° farther to the north. It has its highest amplitude in southeastern Germany; hence, we denominate it the Eastern Alpine Northern Anomaly (Figure 12).

A thickened crust at the southern boundary of the European plate is shown in profile G (Figures 10 and 12). However, no clear slab-like structure can be seen below this area and only a moderate increase in shear velocity is visible below 100 km depth. The small downgoing high-velocity anomaly in profile I at 700 km could be attributed either to the Adriatic or to the European plate.

Dinarides. Caused by the limited station coverage in the Dinarides south of 45°N, our checkerboard tests indicate a far lower resolution compared to Italy and the Alpine chain (Figure 6). The mapped structures have therefore a higher uncertainty.

Two main fast anomalies are observable in our model, separated by a very small structure of reduced velocities at 45.5°N, between 80 and 130 km depth which may be linked to the larger Pannonian anomaly. South of 45°N, the fast anomaly follows closely the limit of the Adriatic plate with a pronounced increase in shear velocity directly beneath the Moho and moderate increase below 100 km depth (Figure 13).

The Adriatic slab under the Dinarides appears almost vertical in our models, with a slight inclination toward the northeast. It is lower in amplitude than the slab in the central Alps but can be followed as moderate high-velocity anomaly down to 150 km depth. However, because of the mentioned lack of resolution of our model in this area, comparisons with the Alpine structures should be made with care.

Apennines. The mantle structure under Italy north of 43°N is characterized by a fast anomaly following the Apenninic front which is itself separated by a sharp boundary from the low-velocity western Mediterranean mantle (Figures 12 and 13, maps). South of 43°N, a gap in the fast anomaly becomes evident. This gap extends southward to about 41°N. The Apenninic slab is always vertical at depth in the profiles of Figure 12, sometimes with a slight tendency of dipping in the opposite direction of the inferred subduction direction (Figure 13).

5. Discussion

The geological features that we believe to have resolved are most sharply defined under the central Alps, where the fast, vertical anomaly is continuous from the European Moho down to 200 km depth. Before the onset of continental collision in the Alps at 35 Ma, Adria acted as upper and Europe as lower plate. It has been proposed that the central Alpine slab steepened during the continental collision because the convergence rate decreased while the slab-pull remained strong (Kissling, 2008; Singer et al., 2014). This process may finally result in the break-off of the oceanic slab fragment. This would explain the very steep geometry of the slab as we imaged it under the central Alps. There is no indication of a slab break-off in the top 200 km, which is in agreement with body wave tomographic images (Lippitsch et al., 2003; Koulakov et al., 2009; Mitterbauer et al., 2011; Zhao et al., 2016). Collisional shortening in the central Alps is of the order of minimum 120 km (Schmid et al., 1996). Therefore, assuming that the slab break-off took place at the ocean-continent transition (Blanckenburg & Davies, 1995), it would be localized at depths greater 150 km. The area showing the continuous central Alpine slab is limited toward the west at 46°N and toward the east at 12°E, close to the Giudicarie line (Figure 12). The spatial correlation of the eastward termination of the slab and the Giudicarie line has also been observed in the tomographic model of Zhao et al. (2016) and is similar to the structures modeled by Mitterbauer et al. (2011). The pronounced difference in anomaly strength indicates a different evolution of the central Alpine subduction compared to the western and eastern Alps.

The low velocities assessed in our images beneath the western Alps, under the Ivrea zone, point to a shallow (below 100 km) break-off of the European slab (Figure 12, sections A and B). The detached part of the slab could cause the fast anomaly in profiles A and B below 100 km underneath the Po basin but more likely corresponds to the Apenninic slab (Figure 12) or a interaction of both (Zhao et al., 2016). The model of Lippitsch et al. (2003) supports the hypothesis of a slab break-off under the western Alps: they image a slab sitting between 150 and 350 km depth, separated from the overlying European lithosphere by low velocities. This contradicts the results of Zhao et al. (2016), who find a thin (50 km) slab linking the deeper anomaly with the lithosphere. Such a thin link at 100 km depth is at the resolution limit of our model (Figure 7d) but is unlikely given the low-velocity structure in our model, located along the termination of the shallow slab under the western Alps. The thin link between the lithosphere and the deeper slab is also not present in the southern western Alps in the model of Zhao et al. (2016), strengthening our argument in favor of a detached European slab under the western Alps.

From the difference between central and eastern Alpine anomaly, we infer that also under the eastern Alps the European slab is partially or completely broken off. Earlier works show a pronounced high-velocity anomaly under the eastern Alps: Lippitsch et al. (2003) image a slab down to 250 km which they attribute to the subduction of the Adriatic plate. The models of Dando et al. (2011) and Mitterbauer et al. (2011) show a slab down to at least 400 km which is detached from the mantle lithosphere toward the east. They interpret the slab to be of European origin. Zhao et al. (2016) report a continuous slab down to 500 km which they argue is showing the subduction of the Adriatic plate. Despite these differences, they all agree that the v_p anomaly between approximately 70 and 150 km depth is less pronounced compared to the deeper parts of the slab. We propose that the apparent vertical continuity of the slab from some of the body wave models may be caused by vertical smearing but that the European slab is broken off. Zhao et al. (2016) suggest that the amplitude of the deep anomaly under the eastern Alps, below 150 km, is half as high as in the central Alps. These findings are consistent with the difference in anomaly strength between the central and eastern Alps in our model. The moderately increased velocities under the eastern Alps in our model (about 1%, compared to 3% under the central Alps) may be caused either by vertical smearing from a deeper-lying European slab or by beginning subduction of the Adriatic lithosphere. The Adriatic subduction is characterized by a less pronounced anomaly as observed under the Apennines and Dinarides. An interaction of partially broken off European slab and shallow Adriatic subduction could also explain the observed anomaly pattern.

There is an almost continuous transition between the eastern Alpine anomaly and the Dinaric slab. The complexity of the eastern Alpine structures is further increased by the presence of the subparallel Eastern Alpine Northern Anomaly, north of the eastern Alps.

The previously reported slab gap (e.g., Piromallo & Morelli, 2003) in the Dinaric subduction zone below 150 km is also visible in our model (Figure 12, profiles H and K). At shallower depth, only a thin zone (80 km) of low velocities cuts through the Dinaric slab between 80 and 150 km depth (45°N–45.6°N). The gap at depth is inferred to result from the rollback of the subduction along the Dinaric-Hellenic front in combination with magmatism and extension in the Pannonian Basin which started at about 20 Ma ago (Matenco & Radivojević, 2012). The extensional dynamics have probably started with a break-off of the Adriatic slab under the Dinarides during the beginning of the continental collision 35 Ma ago, causing the rise of asthenospheric mantle material (Handy et al., 2015; Kovács et al., 2012).

Our model shows that Dinaric and Apenninic slabs are only 200 km apart along profile D (Figure 13). Both show a significantly weaker anomaly compared to the central Alpine slab (Figure 12, profiles C–F, Figure 13). The less pronounced anomaly may be caused by the large adjacent low-velocity domains under the Mediterranean Sea and the Pannonian Basin, given the volume-averaging properties of long period surface waves and the smoothing in the phase velocity maps.

The Apenninic slab in our model is vertical and is interrupted by a gap between 42°N and 43°N. Apenninic slab rollback (Vignaroli et al., 2008) is compatible with the very steep dip. A similar geometry is observable in the body wave tomographic models of Koulakov et al. (2009) and Zhao et al. (2016) that show vertical subduction under the northern Apennines down to 150 km depth and a moderate dip to the southwest at greater depths. Body wave tomography indicates further that the slab gap attains 200 km depth, but the slab is continuous at greater depth (Koulakov et al., 2009; Wortel & Spakman, 2000; Zhao et al., 2016). The gap may indicate a beginning slab tear or intrusion of hot and slow mantle material. Carminati and Doglioni (2012) remark that between 41°N and 42°N the main transition between the lower convergence rates

of the northern Apennines and the higher ones of southern Apennines takes place. This is also expressed in orogenic magmatism in the north versus backarc-related magmatism in the south. The different convergence rates may be related to the slab tearing below.

6. Conclusions

The main goal of this work is to study the crust and mantle structures of the Alpine, Dinaric, and Apenninic collision zones by a combination of AN- and EQ-based surface wave data. A large data set of Rayleigh and Love wave phase velocity measurements is compiled and used to derive high-resolution phase velocity maps. Finally, we apply a nonlinear model search to resolve the shear velocity structure of the uppermost 200 km under the Alps, Apennines, and northern Dinarides. Our model is unique in its combination of wide aperture and high lateral resolution in the crust (~25 km) and its continuity from the surface to the upper mantle. This allows us to make comparisons with detailed crustal studies from receiver functions and reflection seismics (Figure 10), and, at mantle depths, to characterize the geometry of the main subducted slabs, comparing them to inferences from earlier body wave tomography models.

Our crustal model is characterized by a number of high-resolution features that are naturally associated with sedimentary basins, midcrustal anomalies, and the crustal thickness, in agreement with independent observations. We infer that it could serve as a v_s reference model for the Alpine crust in future studies.

We derive a sharp Moho boundary from the applied model search that is in good agreement with previous receiver function studies. We show that in situations where the v_s contrast between crust and mantle is high, our results from surface waves differ by less than 5 km from receiver function measurements.

We find evidence for the Ivrea geophysical anomaly in the western and central Alps, extending approximately along the Periadriatic Fault from 44.5°N to 46°N (Figure 9). We suggest that under the western Alps the subduction slab is detached below 100 km depth. This finding is based on a low-velocity zone that separates the European slab in the shallow mantle from a deeper, fast anomaly below 150 km depth. This is clearly different from the central Alpine slab which is broad and continuous down to 200 km depth and shows a pronounced anomaly. Also, in the eastern Alps we find a fast anomaly signature that is clearly distinct from the central Alps. We infer that the European slab is detached under the eastern Alps. Results from body wave tomography indicate that a detached European slab may be present at depth greater than 150 km (e.g., Mitterbauer et al., 2011). We find no unambiguous indication of an Adriatic subduction under the eastern Alps, but we remark that the moderate positive velocity anomaly could be interpreted this way. South of the Periadriatic Fault, we interpret the fast anomaly as Adriatic subduction under the Dinarides.

We describe the Eastern Alpine Northern Anomaly, subparallel to the eastern Alps toward the north. This represents a potential area for further studies in order to determine its origin.

The Dinaric slab in our model extends to approximately 150 km depth, while no significant velocity heterogeneity is found at larger depths in the same area. A thin zone of reduced velocities is also identified at shallower depths at 45°N. The slab gap in the Apennines is clearly present in our models and is in agreement with previous, body wave tomography studies (e.g., Zhao et al., 2016). It can be explained in terms of differential convergence rates between northern and southern Apennines (Carminati & Doglioni, 2012) and could show the onset of a slab tearing.

Our study shows that the combination of AN and EQ surface wave data enhances the resolution of both crust and upper-mantle seismic velocity structure. Teleseismic body waves generally lack resolution in the lithosphere and asthenosphere and are very dependent on crustal corrections, while local earthquake tomography, reflection seismics, or AN methods only provide robust constraints within the crust. A significant advantage afforded by our model is the continuously good coverage down to 200 km depth. Future efforts to improve seismic models in the critical, lithosphere-asthenosphere depth range would profit from the joint inversion of surface wave data like ours and teleseismic body wave data. The depth extent of subducting slabs under the Alps could thus be verified down to the transition zone.

References

- Aki, K. (1957). Space and time spectra of stationary stochastic waves, with special reference to microtremors. *Bulletin of the Earthquake Research Institute*, 35, 411–451.
- Aki, K., & Richards, P. G. (Eds.) (2002). *Quantitative seismology* (pp. 704). Sausalito, CA: University Science Books.

Acknowledgments

We thank the Associate Editor and two anonymous reviewers for their helpful comments. We are grateful to all the network operators providing data to the EIDA archive (<http://www.orfeus-eu.org/eida>). We thank the makers of Obspy (Beyreuther et al., 2010) and Geopsy (www.geopsy.org). Graphics were created with Python Matplotlib and GMT (Wessel & Smith, 1998). A. E. acknowledges funding from the German Academic Exchange Service (DAAD). L. B. has received funding from the European Union's Horizon 2020 research and innovation program under the Marie Skłodowska-Curie grant agreement 641943. This model can be found in supporting information Data Set S1, or it can be downloaded from <http://hestia.lgs.jussieu.fr/%7EBoschil/downloads.html>.

- Auer, L., Boschi, L., Becker, T., Nissen-Meyer, T., & Giardini, D. (2014). Savani: A variable resolution whole-mantle model of anisotropic shear velocity variations based on multiple data sets. *Journal of Geophysical Research: Solid Earth*, *119*, 3006–3034. <https://doi.org/10.1002/2013JB010773>
- Babuska, V., & Cara, M. (1991). *Seismic anisotropy in the Earth* (Vol. 10). Netherlands: Springer Science & Business Media.
- Béthoux, N., Sue, C., Paul, A., Virieux, J., Fréchet, J., Thouvenot, F., & Cattaneo, M. (2007). Local tomography and focal mechanisms in the south-western Alps: Comparison of methods and tectonic implications. *Tectonophysics*, *432*(1), 1–19.
- Beyreuther, M., Barsch, R., Krischer, L., Megies, T., Behr, Y., & Wassermann, J. (2010). ObsPy: A Python toolbox for seismology. *Seismological Research Letters*, *81*(3), 530–533.
- Bigi, G., Cosentino, D., Parotto, M., Sartori, R., & Scandone, P. (1990). Structural model of Italy, 1:500.000. *Quaderni della Ricerca Scientifica - CNR*, *114*(3).
- Blanckenburg, F., & Davies, J. H. (1995). Slab breakoff: A model for syncollisional magmatism and tectonics in the Alps. *Tectonics*, *14*(1), 120–131.
- Bleibinhaus, F., & Gebrande, H. (2006). Crustal structure of the Eastern Alps along the TRANSALP profile from wide-angle seismic tomography. *Tectonophysics*, *414*(1), 51–69.
- Bois, C., & Party, E. S. (1990). Major geodynamic processes studied from the ECORS deep seismic profiles in France and adjacent areas. *Tectonophysics*, *173*(1–4), 397–410.
- Boschi, L. (2006). Global multiresolution models of surface wave propagation: Comparing equivalently regularized born and ray theoretical solutions. *Geophysical Journal International*, *167*(1), 238–252.
- Boschi, L., & Dziewonski, A. M. (1999). High- and low-resolution images of the Earth's mantle: Implications of different approaches to tomographic modeling. *Journal of Geophysical Research*, *104*(B11), 25,567–25,594.
- Bousquet, R., Goffé, B., Henry, P., Le Pichon, X., & Chopin, C. (1997). Kinematic, thermal and petrological model of the Central Alps: Lepontine metamorphism in the upper crust and eclogitisation of the lower crust. *Tectonophysics*, *273*(1), 105–127.
- Carminati, E., & Doglioni, C. (2012). Alps vs. Apennines: The paradigm of a tectonically asymmetric Earth. *Earth-Science Reviews*, *112*(1), 67–96.
- Castellarin, A., Nicolich, R., Fantoni, R., Cantelli, L., Sella, M., & Selli, L. (2006). Structure of the lithosphere beneath the Eastern Alps (southern sector of the TRANSALP transect). *Tectonophysics*, *414*(1), 259–282.
- Dando, B., Stuart, G., Houseman, G., Hegedüs, E., Brückl, E., & Radovanović, S. (2011). Teleseismic tomography of the mantle in the Carpathian-Pannonian region of central Europe. *Geophysical Journal International*, *186*(1), 11–31.
- de Vos, D., Paulssen, H., & Fichtner, A. (2013). Finite-frequency sensitivity kernels for two-station surface wave measurements. *Geophysical Journal International*, *194*(2), 1042–1049.
- Diehl, T., Husen, S., Kissling, E., & Deichmann, N. (2009). High-resolution 3-D P-wave model of the Alpine crust. *Geophysical Journal International*, *179*(2), 1133–1147.
- Dziewonski, A. M., & Anderson, D. L. (1981). Preliminary reference Earth model. *Physics of the Earth and Planetary Interiors*, *25*(4), 297–356.
- Ekström, G. (2011). A global model of Love and Rayleigh surface wave dispersion and anisotropy, 25–250 s. *Geophysical Journal International*, *187*(3), 1668–1686.
- Ekström, G., Abers, G. A., & Webb, S. C. (2009). Determination of surface-wave phase velocities across USArray from noise and Aki's spectral formulation. *Geophysical Research Letters*, *36*, L18301. <https://doi.org/10.1029/2009GL039131>
- Faccenna, C., Becker, T. W., Auer, L., Billi, A., Boschi, L., Brun, J. P., ... Serpelloni, E. (2014). Mantle dynamics in the Mediterranean. *Reviews of Geophysics*, *52*, 283–332. <https://doi.org/10.1002/2013RG000444>
- Fry, B., Deschamps, F., Kissling, E., Stehly, L., & Giardini, D. (2010). Layered azimuthal anisotropy of Rayleigh wave phase velocities in the European Alpine lithosphere inferred from ambient noise. *Earth and Planetary Science Letters*, *297*(1), 95–102.
- Geissler, W. H., Sodoudi, F., & Kind, R. (2010). Thickness of the central and eastern European lithosphere as seen by S receiver functions. *Geophysical Journal International*, *181*(2), 604–634.
- Giacomuzzi, G., Civalleri, M., De Gori, P., & Chiarabba, C. (2012). A 3D Vs model of the upper mantle beneath Italy: Insight on the geodynamics of central Mediterranean. *Earth and Planetary Science Letters*, *335*, 105–120.
- Giacomuzzi, G., Chiarabba, C., & De Gori, P. (2011). Linking the Alps and Apennines subduction systems: New constraints revealed by high-resolution teleseismic tomography. *Earth and Planetary Science Letters*, *301*(3), 531–543.
- Goes, S., Govers, R., & Vacher, P. (2000). Shallow mantle temperatures under Europe from P and S wave tomography. *Journal of Geophysical Research*, *105*(B5), 11,153–11,169.
- Gueguen, E., Doglioni, C., & Fernandez, M. (1997). Lithospheric boudinage in the Western Mediterranean back-arc basin. *Terra Nova*, *9*(4), 184–187.
- Handy, M. R., Schmid, S. M., Bousquet, R., Kissling, E., & Bernoulli, D. (2010). Reconciling plate-tectonic reconstructions of Alpine Tethys with the geological–geophysical record of spreading and subduction in the Alps. *Earth-Science Reviews*, *102*(3), 121–158.
- Handy, M. R., Ustaszewski, K., & Kissling, E. (2015). Reconstructing the Alps–Carpathians–Dinarides as a key to understanding switches in subduction polarity, slab gaps and surface motion. *International Journal of Earth Sciences*, *104*(1), 1–26.
- Hirn, A., Nadir, S., Thouvenot, F., Nicolich, R., Pellis, G., ... Ecors-Crop Deep Seismic Sounding Group (1989). Mapping the Moho of the Western Alps by wide-angle reflection seismics. *Tectonophysics*, *162*(3–4), 193–202.
- Hirn, A., Damotte, B., Torreilles, G., & Party, E. S. (1987). Crustal reflection seismics: The contributions of oblique, low frequency and shear wave illuminations. *Geophysical Journal International*, *89*(1), 287–296.
- International Seismological Centre (2014). *On-line bulletin*. Thatcham, UK: International Seismological Centre. Retrieved from <http://www.isc.ac.uk>
- Kästle, E. D., Soomro, R., Weemstra, C., Boschi, L., & Meier, T. (2016). Two-receiver measurements of phase velocity: Cross-validation of ambient-noise and earthquake-based observations. *Geophysical Journal International*, *207*(3), 1493–1512.
- Kissling, E. (1984). In J.-J. Wagner & S. Müller (Eds.), *Three-dimensional gravity model of the northern Ivrea-Verbano Zone* (Vol. 21, pp. 55–61). Geomagnetic and Gravimetric Studies of the Ivrea Zone: Matér. Géol. Suisse. Géophys.
- Kissling, E. (2008). Deep structure and tectonics of the Valais—and the rest of the Alps. *Bulletin fuer Angewandte Geologie*, *13*(2), 3–10.
- Kohler, A., Weidle, C., & Maupin, V. (2012). Crustal and uppermost mantle structure of southern Norway: Results from surface wave analysis of ambient seismic noise and earthquake data. *Geophysical Journal International*, *191*(3), 1441–1456.
- Koulakov, I., Kaban, M., Tesauro, M., & Cloetingh, S. (2009). P- and S-velocity anomalies in the upper mantle beneath Europe from tomographic inversion of ISC data. *Geophysical Journal International*, *179*(1), 345–366.
- Kovach, R. L. (1978). Seismic surface waves and crustal and upper mantle structure. *Reviews of Geophysics*, *16*(1), 1–13.

- Kovács, I., Falus, G., Stuart, G., Hidas, K., Szabó, C., Flower, M., ... Zilahi-Sebess, L. (2012). Seismic anisotropy and deformation patterns in upper mantle xenoliths from the central Carpathian–Pannonian region: Asthenospheric flow as a driving force for Cenozoic extension and extrusion? *Tectonophysics*, 514, 168–179.
- Kummerow, J., Kind, R., Oncken, O., Giese, P., Ryberg, T., Wylegalla, K., ... Transalp Working Group (2004). A natural and controlled source seismic profile through the Eastern Alps: TRANSALP. *Earth and Planetary Science Letters*, 225(1), 115–129.
- Legendre, C., Meier, T., Lebedev, S., Friederich, W., & Viereck-Gotte, L. (2012). A shear wave velocity model of the European upper mantle from automated inversion of seismic shear and surface waveforms. *Geophysical Journal International*, 191(1), 282–304.
- Li, C., van der Hilst, R. D., Engdahl, E. R., & Burdick, S. (2008). A new global model for *P* wave speed variations in Earth's mantle. *Geochemistry, Geosystems*, 9, Q05018. <https://doi.org/10.1029/2007GC001806>
- Lin, F.-C., Moschetti, M. P., & Ritzwoller, M. H. (2008). Surface wave tomography of the western United States from ambient seismic noise: Rayleigh and Love wave phase velocity maps. *Geophysical Journal International*, 173(1), 281–298.
- Lippitsch, R., Kissling, E., & Ansoerge, J. (2003). Upper mantle structure beneath the Alpine orogen from high-resolution teleseismic tomography. *Journal of Geophysical Research*, 108(B8), 2376. <https://doi.org/10.1029/2002JB002016>
- Lombardi, D., Braunmiller, J., Kissling, E., & Giardini, D. (2008). Moho depth and Poisson's ratio in the Western-Central Alps from receiver functions. *Geophysical Journal International*, 173(1), 249–264.
- Lüschen, E., Lammerer, B., Gebrande, H., Millahn, K., Nicolich, R., & TRANSALP Working Group (2004). Orogenic structure of the Eastern Alps, Europe, from TRANSALP deep seismic reflection profiling. *Tectonophysics*, 388(1), 85–102.
- Matenco, L., & Radivojević, D. (2012). On the formation and evolution of the Pannonian Basin: Constraints derived from the structure of the junction area between the Carpathians and Dinarides. *Tectonics*, 31, TC6007. <https://doi.org/10.1029/2012TC003206>
- Meier, T., Dietrich, K., Stöckhert, B., & Harjes, H.-P. (2004). One-dimensional models of shear wave velocity for the eastern Mediterranean obtained from the inversion of Rayleigh wave phase velocities and tectonic implications. *Geophysical Journal International*, 156(1), 45–58.
- Meier, T., Soomro, R., Viereck, L., Lebedev, S., Behrmann, J. H., Weidle, C., ... Hanemann, R. (2016). Mesozoic and Cenozoic evolution of the Central European lithosphere. *Tectonophysics*, 692, 58–73.
- Mitterbauer, U., Behm, M., Brückl, E., Lippitsch, R., Guterch, A., Keller, G. R., ... Šumanovac, F. (2011). Shape and origin of the East-Alpine slab constrained by the ALPASS teleseismic model. *Tectonophysics*, 510(1), 195–206.
- Molinari, I., Argnani, A., Morelli, A., & Basini, P. (2015). Development and testing of a 3D seismic velocity model of the Po Plain sedimentary basin, Italy. *Bulletin of the Seismological Society of America*, 105(2A), 753–764.
- Muyzert, E., & Snieder, R. (2000). An alternative parameterisation for surface waves in a transverse isotropic medium. *Physics of the Earth and Planetary Interiors*, 118(1), 125–133.
- Oeberseder, T., Behm, M., Kovács, I., & Falus, G. (2011). A seismic discontinuity in the upper mantle between the Eastern Alps and the Western Carpathians: Constraints from wide angle reflections and geological implications. *Tectonophysics*, 504(1), 122–134.
- Paige, C. C., & Saunders, M. A. (1982). LSQR: An algorithm for sparse linear equations and sparse least squares. *ACM transactions on mathematical software*, 8(1), 43–71.
- Pfiffner, O.-A. (1992). *Blundell, DJ, Freeman, R, Mueller, S and Button, S: A continent revealed: The European geotraverse, structure and dynamic evolution*. Cambridge, UK: Cambridge University Press.
- Pfiffner, O.-A., Lehner, P., Heitzmann, P., Mueller, S., & Steck, A. (1997). *Deep structure of the Swiss Alps*. Basel, Switzerland: Springer.
- Piomallo, C., & Morelli, A. (2003). *P* wave tomography of the mantle under the Alpine-Mediterranean area. *Journal of Geophysical Research*, 108(B2), 2065. <https://doi.org/10.1029/2002JB001757>
- Roure, F., Choukroune, P., & Polino, R. (1996). Deep seismic reflection data and new insights on the bulk geometry of mountain ranges. *Comptes rendus de l'Académie des sciences. Série 2. Sciences de la terre et des planètes*, 322(5), 345–359.
- Sambridge, M. (1999). Geophysical inversion with a neighbourhood algorithm—II. Appraising the ensemble. *Geophysical Journal International*, 138(3), 727–746.
- Sato, Y. (1955). Analysis of dispersed surface waves by means of Fourier transform I. *Bulletin of the Earthquake Research Institute, Tokyo Univ.*, 33, 33–47.
- Schmid, S., & Kissling, E. (2000). The arc of the western Alps in the light of geophysical data on deep crustal structure. *Tectonics*, 19(1), 62–85.
- Schmid, S. M., Pfiffner, O.-A., Froitzheim, N., Schönborn, G., & Kissling, E. (1996). Geophysical-geological transect and tectonic evolution of the Swiss-Italian Alps. *Tectonics*, 15(5), 1036–1064.
- Seiberlich, C., Ritter, J., & Wawerzinek, B. (2013). Topography of the lithosphere–asthenosphere boundary below the Upper Rhine Graben Rift and the volcanic Eifel region, Central Europe. *Tectonophysics*, 603, 222–236.
- Shen, W., Ritzwoller, M. H., & Schulte-Pelkum, V. (2013). A 3-D model of the crust and uppermost mantle beneath the Central and Western US by joint inversion of receiver functions and surface wave dispersion. *Journal of Geophysical Research: Solid Earth*, 118, 262–276. <https://doi.org/10.1029/2012JB009602>
- Singer, J., Diehl, T., Husen, S., Kissling, E., & Duret, T. (2014). Alpine lithosphere slab rollback causing lower crustal seismicity in northern foreland. *Earth and Planetary Science Letters*, 397, 42–56.
- Soomro, R., Weidle, C., Cristiano, L., Lebedev, S., Meier, T., & PASSEQ Working Group (2016). Phase velocities of Rayleigh and Love waves in central and northern Europe from automated, broad-band, interstation measurements. *Geophysical Journal International*, 204(1), 517–534.
- Spada, M., Bianchi, I., Kissling, E., Agostinetti, N. P., & Wiemer, S. (2013). Combining controlled-source seismology and receiver function information to derive 3-D Moho topography for Italy. *Geophysical Journal International*, 194(2), 1050–1068.
- Spakman, W., & Wortel, R. (2004). A tomographic view on western Mediterranean geodynamics. In W. Cavazza, et al. (Eds.), *The TRANSMED atlas, The Mediterranean region from crust to mantle* (pp. 31–52). Berlin, Heidelberg: Springer.
- Stampfli, G. M., & Borel, G. (2002). A plate tectonic model for the Paleozoic and Mesozoic constrained by dynamic plate boundaries and restored synthetic oceanic isochrons. *Earth and Planetary Science Letters*, 196(1), 17–33.
- Stehly, L., Fry, B., Campillo, M., Shapiro, N., Guilbert, J., Boschi, L., & Giardini, D. (2009). Tomography of the Alpine region from observations of seismic ambient noise. *Geophysical Journal International*, 178(1), 338–350.
- Thouvenot, F., Paul, A., Frechet, J., Béthoux, N., Jenatton, L., & Guiguet, R. (2007). Are there really superposed Mohos in the southwestern Alps? New seismic data from fan-profiling reflections. *Geophysical Journal International*, 170(3), 1180–1194.
- TRANSALP Working Group, Gebrande, H., Lüschen, E., Bopp, M., Bleibinhaus, F., Lammerer, B., ... Bernabini, M. (2002). First deep seismic reflection images of the Eastern Alps reveal giant crustal wedges and transcrustal ramps. *Geophysical Research Letters*, 29(10), 1452. <https://doi.org/10.1029/2002GL014911>
- Verbeke, J., Boschi, L., Stehly, L., Kissling, E., & Michelini, A. (2012). High-resolution Rayleigh-wave velocity maps of central Europe from a dense ambient-noise data set. *Geophysical Journal International*, 188(3), 1173–1187.

- Vignaroli, G., Faccenna, C., Jolivet, L., Piromallo, C., & Rossetti, F. (2008). Subduction polarity reversal at the junction between the Western Alps and the Northern Apennines, Italy. *Tectonophysics*, *450*(1), 34–50.
- Ward, K. M., Zandt, G., Beck, S. L., Wagner, L. S., & Tavera, H. (2016). Lithospheric structure beneath the northern Central Andean Plateau from the joint inversion of ambient noise and earthquake-generated surface waves. *Journal of Geophysical Research: Solid Earth*, *121*, 8217–8238. <https://doi.org/10.1002/2016JB013237>
- Wathelet, M. (2005). *Array recordings of ambient vibrations: Surface-wave inversion* (PhD dissertation). Liège University, 161.
- Wathelet, M. (2008). An improved neighborhood algorithm: Parameter conditions and dynamic scaling. *Geophysical Research Letters*, *35*, L09301. <https://doi.org/10.1029/2008GL033256>
- Wessel, P., & Smith, W. H. (1998). The Generic Mapping Tools. *Eos, Transactions American Geophysical Union*, *79*, 579.
- Wortel, M., & Spakman, W. (2000). Subduction and slab detachment in the Mediterranean-Carpathian region. *Science*, *290*(5498), 1910–1917.
- Yang, Y., Li, A., & Ritzwoller, M. H. (2008). Crustal and uppermost mantle structure in southern Africa revealed from ambient noise and teleseismic tomography. *Geophysical Journal International*, *174*(1), 235–248.
- Yang, Y., Ritzwoller, M. H., Lin, F.-C., Moschetti, M., & Shapiro, N. M. (2008). Structure of the crust and uppermost mantle beneath the western United States revealed by ambient noise and earthquake tomography. *Journal of Geophysical Research*, *113*, B12310. <https://doi.org/10.1029/2008JB005833>
- Yao, H., van Der Hilst, R. D., & Maarten, V. (2006). Surface-wave array tomography in SE Tibet from ambient seismic noise and two-station analysis—I. Phase velocity maps. *Geophysical Journal International*, *166*(2), 732–744.
- Zhao, L., Paul, A., Guillot, S., Solarino, S., Malusà, M. G., Zheng, T., ... Wang, Q. (2015). First seismic evidence for continental subduction beneath the Western Alps. *Geology*, *43*(9), 815–818.
- Zhao, L., Paul, A., Malusà, M. G., Xu, X., Zheng, T., Solarino, S., ... Zhu, R. (2016). Continuity of the Alpine slab unraveled by high-resolution P wave tomography. *Journal of Geophysical Research: Solid Earth*, *121*, 8720–8737. <https://doi.org/10.1002/2016JB013310>
- Zhou, L., Xie, J., Shen, W., Zheng, Y., Yang, Y., Shi, H., & Ritzwoller, M. H. (2012). The structure of the crust and uppermost mantle beneath South China from ambient noise and earthquake tomography. *Geophysical Journal International*, *189*(3), 1565–1583.
- Zhu, H., Bozdağ, E., Peter, D., & Tromp, J. (2012). Structure of the European upper mantle revealed by adjoint tomography. *Nature Geoscience*, *5*(7), 493–498.
- Ziegler, P., Schumacher, M., Dèzes, P., Van Wees, J.-D., & Cloetingh, S. (2004). Post-Variscan evolution of the lithosphere in the Rhine Graben area: Constraints from subsidence modelling. *Geological Society, London, Special Publications*, *223*(1), 289–317.